

## ABSTRACT

Jimenez, Kianna. Advanced Nanoporous Materials for Magnetic Resonance of Biomacromolecules. (Under the direction of Dr. Alex I. Smirnov).

Anodic aluminum oxide (AAO) membranes with macroscopically aligned nanopore structures have inspired much interest in the nanomaterial and nanotechnology field. With the ability to tune the AAO nanopore properties through enhanced anodization and chemical methods, these structures have become suitable for many applications, including an emerging field of bionanotechnology. One such application is the use of AAO membranes as templates to achieve unique macroscopic alignment of membrane lipids and membrane-embedded proteins folded into solvent-accessible nanotubular structures.

Lipid bilayer membranes play a pivotal role in biology, including energy transduction events essential for biological function. While some of these roles are undoubtedly structural in nature, others may be related to the electronic structure, as indicated by the need for lipids with an anionic headgroup, such as PG lipids, for photosynthesis. Magnetic resonance methods are known to offer a wealth of data on the structure of these lipid systems. Previously, substrate-supported lipid bilayers were developed to investigate the arrangement and functionality of lipid membranes by magnetic resonance. However, the above-mentioned lipid membrane mimetics could only be formed from a relatively narrow class of lipids and lipid-like molecules and have several other restrictions such as temperature, pH, ionic strength, etc. More recently, anodic aluminum oxide membranes with tunable diameters from ca. 40 to 200 nm were utilized to promote the self-assembly of lipid nanotubular bilayers inside the pores. The macroscopic alignment of the lipid assemblies provided by such structures assists in characterizing the biophysical properties of nanopore-confined molecules by magnetic resonance methods such as NMR and EPR.

The primary aims of this research project were (1) to advance nanoporous AAO fabrication methods by optimization of anodization techniques and exploring different pore surface modification methods with the goals of making such nanostructures conductive or semiconductive and (2) to investigate how surface electrostatic properties of nanotubular lipid bilayers confined in such nanopores are affected by the AAO fabrication procedures and pore geometry. For the latter, spin-labeling EPR of pH-sensitive stable nitroxide radicals was employed. Using an improved anodization method in H<sub>3</sub>PO<sub>4</sub>, we present the results of enhanced fabrication of AAO by mild anodization and pulse anodization to produce larger uniformly ordered nanopores of diameter  $d \approx 450$  nm. Such large pores are considered essential for incorporating large membrane protein complexes such as Photosystem I and Photosystem II. Electroless deposition of conductive material into the AAO was also investigated to promote conductivity of the AAO substrate. It was found that there was insufficient deposition of the materials within the nanopores, which resulted in no conductivity. Finally, we employed spin-labeling EPR and pH-sensitive nitroxide radicals to assess the surface electrostatics of lipid bilayers through substrate-supported self-assembly within the AAO nanopores. A pH-sensitive headgroup labeled phospholipid probe (IMTSL-PTE) synthesized at NCSU was fully integrated into the lipid bilayer. The lipids were deposited onto the substrate, forming cylindrical phospholipid nanotubes in the pores. EPR spectra of such membrane probe reported on its ionization state and, thus, local pH. These spectroscopic data aided in determining the local surface electrostatic potential of nanopore-confined bilayers. By utilizing magnetic resonance approaches, more insight can be gained into the macromolecular dynamics of membrane lipids/proteins.

© Copyright 2023 by Kianna Amari Jimenez

All Rights Reserved

Advanced Nanoporous Materials for Magnetic Resonance of Biomacromolecules

by  
Kianna Amari Jimenez

A dissertation submitted to the Graduate Faculty of  
North Carolina State University  
in partial fulfillment of the  
requirements for the degree of  
Doctor of Philosophy

Chemistry

Raleigh, North Carolina  
2023

APPROVED BY:

---

Dr. Alex I. Smirnov  
Committee Chair

---

Dr. Alexander A. Nevzorov

---

Dr. Thomas Theis

---

Dr. Leslie Sombers

## **DEDICATION**

To my Almighty and Heavenly Father, who loves me and has been with me every step of this journey. To my mother, who has been the best parent I could ever pray for and my main support. To my family and friends, who constantly encouraged me to press on even in the rough times. To every kid thinking about becoming a scientist but believe that it will be too difficult. Finally, to women of color in STEM from the past and in the future who have had to work extremely hard to succeed but still feel less than most times...

This research is dedicated to you.

## **BIOGRAPHY**

Kianna Jimenez was born on February 26, 1995, in New York, New York. As a child, she was very interested in STEM. From an early age, she was immersed in STEM activities and events. In 5th grade, she attended an all-girls engineering summit. During this summit, she was able to catch a glimpse of what she could achieve just by being in the STEM atmosphere. In middle and high school, she attended various science programs to continue learning about the many facets of STEM. One program, in particular, was Photonics Explorers. By participating in this program, she was able to deepen her knowledge of scientific concepts/skills and determine what to potentially pursue in college.

Kianna received a Bachelor of Science in Chemistry and a Bachelor of Arts in Mathematics from Barton College (Wilson, NC) in 2017. As an undergraduate student, she conducted analytical chemistry research, which allowed her to participate in the 2016 Summer REU at the University of Akron, OH. She was also involved in many clubs and organizations on campus that opened her eyes to DEI-related activities. Immediately following her undergraduate degree, she came to NCSU. In 2018, she joined the Smirnov group. Her research centered around physical and analytical chemistry. In addition to her research studies, she participated in CGSA, the chemistry DEI committee, BGSA, ACS, NOBCCChE, SACNAS, and Sube Ritmo (the only Latin dance team at NC State).

## ACKNOWLEDGMENTS

The following people are acknowledged for their contribution to my success:

Dr. Alex Smirnov for being my supportive advisor and allowing me to become a member of  
his research family;

Dr. Alex Nevzorov, Dr. Leslie Sombers, Dr. Thomas Theis, and Dr. Zakiya Leggett for being  
my advisory committee members;

Dr. Maxim Voinov and Dr. Antonin Marek for their willingness to help me with many  
components of my research;

Everyone in the Smirnov/Smirnova/Nevzorov groups for working with me;

Dr. Charles (Chuck) Mooney, King of SEM, for showing me how to use the Verios SEM  
instrument properly;

Family and friends for their ultimate love, care, and support;

My mother for inspiring and motivating me to pursue my dreams/goals;

My Father God for giving me wisdom, discernment, strength, guidance, and knowledge to  
pursue this research and make it to the finish line.

I thank all of you from the bottom of my heart!

## TABLE OF CONTENTS

LIST OF TABLES .....	ix
LIST OF FIGURES .....	x
<b>Chapter 1: Introduction</b> .....	1
1.1. Anodic Aluminum Oxide.....	1
1.1.1. Basic Chemistry and Electrochemistry .....	1
1.1.2. General Structure of Porous AAO .....	2
1.1.3. Fabrication of Highly Ordered Porous AAO .....	3
1.1.4. Surface Modification of AAO with Anodization and Chemical Method .....	4
1.2. Lipids and Lipid Bilayers.....	4
1.2.1. Lipids .....	5
1.2.2. Lipid Bilayers and Electrostatics .....	6
1.2.3. Substrate-supported Lipid Bilayers.....	9
1.3. Electron Paramagnetic Resonance Spectroscopy .....	11
1.3.1. Classical and Quantum Mechanical Description of EPR Spectroscopy .....	12
1.3.2. Hyperfine Interaction .....	14
1.3.3. Site-Directed Spin-labeling EPR .....	16
1.4. Summary of Research .....	19
1.5. References .....	20
<b>Chapter 2: Enhanced Fabrication of AAO</b> .....	25
2.1. Introduction.....	24
2.2. Experimental Section .....	26
2.2.1. Materials and Chemicals.....	26

2.2.2. Mild Anodization of Aluminum in Phosphoric Acid .....	26
2.2.3. Pulse Anodization of Aluminum in Phosphoric Acid.....	27
2.3. Results and Discussion .....	29
2.3.1. AAO Fabrication with Mild Anodization in Phosphoric Acid .....	29
2.3.2. AAO Fabrication with Pulse Anodization in Phosphoric Acid .....	31
2.4. Conclusion .....	33
2.5. References.....	34
<b>Chapter 3: Electroless Deposition into AAO Substrate for Conductivity .....</b>	<b>39</b>
3.1. Introduction.....	37
3.2. Experimental Section.....	38
3.2.1. Materials and Chemicals.....	38
3.2.2. Electroless Deposition of Gold into AAO .....	38
3.2.3. Electroless Deposition of Carbon Char into AAO.....	40
3.2.4. Electroless Deposition of ITO into AAO.....	41
3.2.5. Characterization of AAO Nanopores after Electroless Deposition .....	42
3.3. Results and Discussion .....	42
3.3.1. Gold Deposition .....	43
3.3.2. Carbon Char Deposition .....	45
3.3.3. ITO Deposition .....	47
3.3.4. Conductivity Test.....	51
3.4. Conclusion .....	53
3.5. References.....	54

<b>Chapter 4: Surface Electrostatic Potential of Nanopore-confined Phospholipid Bilayer in High-Temperature Annealed AAO Substrate Revealed by spin-labeling EPR of a pH-sensitive Nitroxide</b> .....	<b>60</b>
4.1. Introduction.....	57
4.2. Experimental Section .....	61
4.2.1. Materials and Chemicals.....	61
4.2.2. Preparation of AAO Substrates with Homogeneous Pore Distribution.....	62
4.2.3. High-Temperature Annealed Nanoporous AAO Substrates.....	63
4.2.4. Preparation of Spin-labeled Lipid Vesicles .....	63
4.2.5. Preparation of Spin-labeled Lipid Vesicles Doped with Gramicidin A .....	63
4.2.6. Preparation of AAO Nanopore-confined POPG MLVs .....	64
4.2.7. pH adjustment of 50mM Phosphate Buffers.....	64
4.2.8. pH adjustment of AAO Nanopore-confined Lipid Bilayers.....	64
4.2.9. EPR Measurements.....	65
4.3. Results and Discussion .....	65
4.3.1. Choice of Lipids for Model Bilayer Systems .....	65
4.3.2. Characterization of the Nanoporous AAO Substrates and Lipid Deposition ....	66
4.3.3. Effect of Unannealed AAO Substrate on EPR spectra of Nanopore-confined Lipid Bilayer.....	69
4.3.4. High-Temperature Annealing of the AAO Substrate .....	71
4.3.5. Determination of Surface Electrostatic Potential of Nanopore-confined POPG Lipid Bilayer in Annealed AAO Substrate.....	73

4.3.6. Determination of Surface Electrostatic Potential of Nanopore-confined POPG Lipid Bilayer Doped with Gramicidin A in Annealed AAO Substrate .....	78
4.4. Conclusion .....	81
4.5. References .....	82
<b>Appendices</b> .....	<b>88</b>
5.1. Appendix A .....	89

## LIST OF TABLES

Table 4.01	<i>Interfacial <math>pK_a^i</math>, polarity-induced and electrostatic shifts, <math>\Delta pK_a^{el}</math>, measured for POPG SUVs doped with 1% IMTSL-PTE at 17 °C. Data was reproduced from ref. [31].</i>	80
Table 4.02	<i>Interfacial <math>pK_a^i</math>, polarity-induced and electrostatic shifts, <math>\Delta pK_a^{el}</math>, measured for POPG SUVs doped with 1% IMTSL-PTE at 17 °C.</i>	83

## LIST OF FIGURES

Figure 1.01	<i>Schematic structure of porous AAO. Reproduced from ref. [3]</i> .....	3
Figure 1.02	Schematic structure of a phospholipid and lipid bilayer. <a href="https://commons.wikimedia.org/wiki/File:0302_Phospholipid_Bilayer.jpg">https://commons.wikimedia.org/wiki/File:0302_Phospholipid_Bilayer.jpg</a> .....	6
Figure 1.03	<i>Common headgroups found in glycerophospholipids and their basic characteristics.</i> <a href="https://phys.libretexts.org/Courses/University_of_California_Davis/UCD%3A_Biophysics_241_-_Membrane_Biology/01%3A_Lipids/1.02%3A_Lipid_Headgroup_Types">https://phys.libretexts.org/Courses/University_of_California_Davis/UCD%3A_Biophysics_241 - Membrane Biology/01%3A Lipids/1.02%3A Lipid Headgroup Types</a> .....	8
Figure 1.04	<i>Schematic representation of the electrostatic potential across a lipid bilayer due to charged groups at the interface. The three major components are displayed: dipole potential, transmembrane potential, and surface potential. Reproduced from ref. [17]</i> .....	9
Figure 1.05	<i>Schematic representation of a substrate-supported lipid bilayer (SSLB). Reproduced from ref. [26]</i> .....	11
Figure 1.06	<i>Zeeman energy level of a free electron (<math>S = \frac{1}{2}</math>) placed in a magnetic field. The blue arrow indicates the energy of the microwave quantum matching the energy splitting between the electron spin substates. Adapted from ref. [32].</i> .....	14
Figure 1.07	<i>Hyperfine splitting of a system consisting of an electron (<math>S=1/2</math>) coupled to a nucleus (<math>I=1/2</math>) with a coupling constant, A. Nuclear Zeeman interaction was neglected for simplicity</i> .....	16
Figure 1.08	<i>Schematic descriptions of (A) isotropic coupling constant and (B) anisotropic hyperfine coupling constant.</i> .....	17
Figure 1.09	<i>Schematic Chemical structure of the nitroxide headgroup of IMTSL spin label and its EPR spectrum with three absorption peaks. Each energy level splits in three levels, and resonance frequency gives rise to three lines in X-band EPR. Reproduced from ref. [35]</i> .....	19
Figure 1.10	<i>EPR line shape as a function of spin label motion. (A) Spin label in dilute solution – fast motion. (B) Spin label attached to a small peptide in solution. (C) Spin-labeled peptide incorporated into a liposome – slow motion. (D) Fully protonated spin label within a liposome, experiencing electrostatic attraction to the bilayer surface. Adapted from ref. [35]</i> .....	19

Figure 2.01 <i>Tunable AAO pore dimensions controlled by the anodization process. Reproduced from ref. [26]</i> .....	26
Figure 2.02 <i>SEM images of (A,C) top and (B,D) bottom sides of the AAO membranes fabricated by mild anodization in H<sub>3</sub>PO<sub>4</sub> at 189 V. (A-B) AAO membrane after 3 h of etching; (C-D) AAO membrane after 7 h etching</i> .....	31
Figure 2.03 <i>SEM images of (A–B) top and (C–D) bottom sides of the AAO membranes fabricated by pulse anodization in H<sub>3</sub>PO<sub>4</sub> at 189 V</i> .....	34
Figure 3.01 <i>IR spectra of silanized AAO membrane after hydrolysis. Peak 5 shows the silanized AAO membrane was hydrolyzed at 1711.51 cm<sup>-1</sup></i> .....	46
Figure 3.02 <i>IR spectra of silanized AAO membrane. Peak 7 shows the AAO membrane was silanized at 1780.94 cm<sup>-1</sup> after treatment in SAPT solution</i> .....	46
Figure 3.03 <i>Deposition of Au-AAO indicated by a color change from (A) white to (B) yellowish-brown</i> .....	47
Figure 3.04 <i>FE-SEM images of Au-AAO deposition on the surface and within the pores. (A–C) Clusters of Au material sit on the surface of the AAO membrane. (D–F) Cross-sectional images show smaller beads of Au material that lie along the walls of the AAO nanopores</i> .....	48
Figure 3.05 <i>Deposition of carbonaceous material into AAO nanopores and development of carbon char indicated by a color change from (A) white to (B) black.</i> .....	49
Figure 3.06 <i>FE-SEM images of carbon char AAO. (A–B) Surface of the AAO membrane with carbon char. (C–E) Cross-section of AAO with carbonaceous material deposited deeper into the nanopores</i> .....	50
Figure 3.07 <i>AAO membrane with aggregation of ITO material on the surface. This major accumulation on the surface inhibits deposition of ITO into the pores</i> .....	53
Figure 3.08 <i>ITO material after dissolving the AAO membrane</i> .....	54
Figure 3.09 <i>Polycarbonate membrane with ITO deposition. Clusters of ITO material remained on the surface without deposition into the pores</i> .....	54
Figure 3.10 <i>Schematic of conductivity test of electroless deposited AAO samples</i> .....	56
Figure 4.01 <i>Chemical structure of POPG lipid</i> .....	69
Figure 4.02 <i>SEM images of top (A–B) and bottom (C–D) sides of the AAO substrate (d≈38 nm, thickness=57 μm)</i> .....	70

Figure 4.03 *Effects of orientation of nanoporous AAO substrate with deposited nanotubular POPG lipid bilayers doped at 1 mol% with IMTSL-PTE vs. magnetic field on X-band EPR spectra. (A) A superposition of the spectra measured with magnetic field perpendicular (red) and parallel (magenta) to the static magnetic field shows small but noticeable changes in the average hyperfine splitting due to the sample macroscopic alignment. These changes are clearly seen at the insert showing a magnified low-field nitrogen hyperfine coupling component for the spectra aligned by the central ( $m_I=0$ ) hyperfine line. These orientation effects are expected to be small for the spin label attached to the lipid polar head via a flexible tether. (B) The difference between the spectra shown in (A) and aligned by adjusting isotropic g-factors and intensities by a least-squares procedure. A consequent reorientation of the AAO substrate perpendicular to the magnetic field yielded an EPR spectrum identical to the one acquired initially: the red and magenta spectra are essentially indistinguishable when superimposed on one another (C) and the difference spectrum (D) shows only random noise. The latter spectra show that minor misalignments of the AAO substrate with respect to magnetic field have no effects on the EPR spectra. All spectra were measured at 17 °C for lipid bilayers equilibrated at pH=7.00. For each of the orientations, 4 different spectra were measured, yielding identical results.....71*

Figure 4.04 *Similar lipid structure of a) a spin-labeled probe and b) a POPG lipid.....73*

Figure 4.05 *Protonation of IMTSL-PTE at the interface of POPG MLVs. Reproduced from ref. [31] .....73*

Figure 4.06 *X-band EPR spectra of AAO substrate-supported POPG doped with 1 mol% IMTSL-PTE acquired for various pH at 17 °C.. .....74*

Figure 4.07 *Effect of high-temperature annealing of nanoporous AAO substrate (A) A superposition of the experimental unannealed AAO spectrum (red) and the unannealed AAO spectrum broadened to 3 Lorentzian points (blue); (B) The difference between the spectra shown in (A) and aligned by adjusting isotropic g-factors and intensities by a least-squares procedure. The red and blue spectra are essentially indistinguishable when superimposed on one another; (C)-(F) spectra measured after annealing the AAO substrate at each temperature. There is a decrease in the AAO background signal as the temperature increases .....75*

Figure 4.08 *X-band EPR spectra of nanopore-confined POPG lipids doped with 1 mol% IMTSL-PTE in AAO substrate annealed at 800 °C acquired for various pH at 17 °C.....76*

Figure 4.09 *Least-squares decomposition of the experimental X-band (9.5 GHz) EPR spectrum of IMTSL-PTE 1 mol%-doped POPG MLVs in annealed AAO at 800 °C acquired at pH=4.08 and 17 °C. (A) Experimental spectrum; Least-squares simulated spectra of (B) nonprotonated and (C) protonated forms of the*

*nitroxide; (D) simulated spectrum; (E) residual of the fit. Adapted from ref. [31].*  
.....78

Figure 4.10 *Titration curve of annealed AAO substrate-supported POPG lipids doped with IMTSL-PTE at 17 °C* .....79

Figure 4.11 *Effect of curvature (vesicle diameter) on the surface electrostatic potential in lipid unilamellar vesicles. Reproduced from ref. [31]* .....80

Figure 4.12 *X-band EPR spectra of nanopore-confined POPG lipids doped with 1 mol% IMTSL-PTE and gramicidin A in AAO substrate annealed at 800 °C acquired for various pH at 17 °C* .....82

Figure 4.13 *Titration curve of annealed AAO substrate-supported POPG lipids doped with IMTSL-PTE and gramicidin A at 17 °C.* .....83

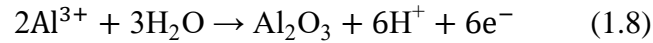
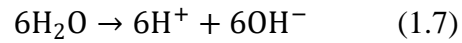
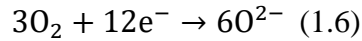
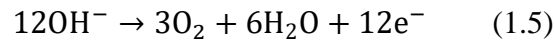
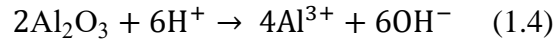
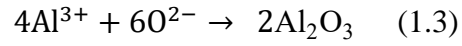
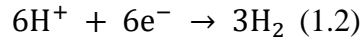
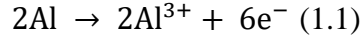
## **CHAPTER 1: INTRODUCTION**

### **1.1. Anodic Aluminum Oxide**

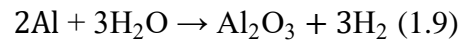
Initially utilized as a surface protectant, anodization of aluminum has been investigated and employed for various applications within industry over the past century. Conventionally, the anodization process consists of a formation of a dense oxide layer on aluminum by electrochemical oxidation in an aqueous solution controlled under potentiostatic conditions [1-3]. This constructed oxide layer, known as anodic aluminum oxide (AAO), has sparked much interest in the field of nanomaterials and nanotechnology due to a favorable combination of morphological, physical, and chemical properties, such as high porosity, stability, resistance, and structural tunability [1-3]. Consequently, numerous advantages of AAO promote further exploration of both enhanced anodization methods and nanoscale applications.

#### **1.1.1. Basic Chemistry and Electrochemistry**

When a metal, such as aluminum (Al), is anodized in an acidic electrolyte under potentiostatic conditions, an anodic oxide layer forms on the metal by the following three ways: diffusion of ions (1) across the metal/oxide interface, (2) through the bulk oxide, and (3) across the oxide/electrolyte interface [3-4]. The diffusive motion of both positive cations ( $\text{Al}^{3+}$ ,  $\text{H}^+$ ) and negative anions ( $\text{O}^{2-}$ ,  $\text{OH}^-$ ) is further accelerated by the high electric field. The essential reactions during the formation of the porous oxide layer are: (1) anodic Al dissolution (Equation 1.1), (2) cathodic hydrogen gas evolution (Equation 1.2), (3) aluminum oxide formation at a metal/oxide boundary (Equation 1.3), (4) aluminum oxide formation at the oxide/electrolyte boundary (Equations 1.4–1.8).



The overall reaction can be presented as follows:



Simultaneously with the oxide formation, a field-enhanced acidic oxide dissolution is also present at the oxide/electrolyte interface. The steady-state growth of the porous oxide layer results from the balance between these two processes. The growth is most intense at the base of the hemispherical-shaped pores, where the intensity of the electric field is the highest due to a high surface curvature.

The oxidation process maintains a certain oxide barrier thickness at the entire pore base and continues to facilitate growth perpendicular to the surface. Growth in any other direction is prevented by the growth of neighboring pores, competing for space. Thus, the vertical growth of the pore walls creates a self-assembled columnar structure that extends from the base of the pore to the surface of the oxide layer.

### 1.1.2. General Structure of Porous AAO

Anodic aluminum oxide is comprised of an array of high-aspect cylindrical parallel nanopores (Figure 1.01). Each nanopore is enclosed in a hexagonal cell with an alignment perpendicular to the metal surface. At the bottom of the film is a thin barrier layer along the metal surface that closes each pore with an approximately hemispherical morphology. Under optimal anodization conditions (anodization regimes), these cells will self-assemble to generate closely packed hexagonal structures with centered pores.

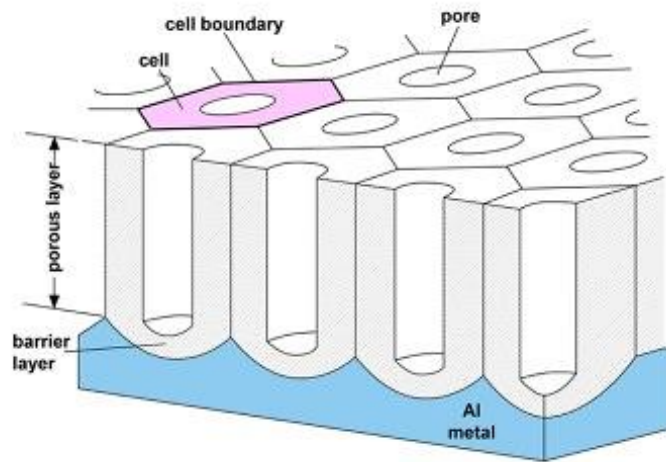


*Figure 1.01 Schematic structure of porous AAO. Reproduced from ref. [3].*

### 1.1.3. Fabrication of Highly Ordered Porous AAO

Porous AAO is typically fabricated using one-step or better two-step anodization methods (previously developed by Masuda et al. [5] from a thin high, purity aluminum foil. The purpose of the second step is to further improve the tight hexagonal packing and organization of the pores. In the first step, pores are initially growing from a mirror-polished metal surface, finding their seeding spots randomly all over the surface. After a certain period, the pores start competing for space with the neighboring pores and self-organizing. This leaves the top surface

somewhat disorganized, while the bottom organization improves with time until large hexagonally organized domains are formed. The second anodization step is nearly identical to the first step but builds upon the achieved bottom pore organization from the first step. When the alumina oxide layer from the first step is removed (e.g., dissolved in a strong acid), the bottom pore hemispheres remain imprinted in the underlying metal. In the second step of anodization, the pore growth no longer seeds pores randomly but instead prefers the pre-patterned depressions where the electric field is the highest. Thus, highly ordered porous AAO can be fabricated with the pores organized on both the top and bottom surfaces [6]. However, stress and other breakdown factors make it possible to still have disorganized pore growth and formation. The two-step process only serves as a framework to optimize the typical pore growth.

#### **1.1.4. Surface Modification of AAO with Anodization and Chemical Method**

AAO membranes have an exceptionally versatile surface and can easily undergo surface modifications using several chemical and physical methods, including but not limited to silane chemistry [7-8], electrochemical and electroless depositions (ECD and ELD) [9-13], and atomic layer deposition (ALD) [14-15]. From these methods, the catalytic and absorption properties of the AAO surface are also altered, impacting the pores' geometry and the selectivity of entering molecules within the pores.

Electrostatic forces are known to play an important role in the interactions of molecules with surfaces. Thus, the determination of electric parameters of the nanopore inner surfaces is highly relevant for both fundamental research and technical application. In recent years, the utilization

of these membranes has broadened in various fields of science and engineering due to the versatility of the AAO surface [16].

## **1.2. Lipids and Lipid Bilayers**

### **1.2.1. Lipids**

Biological membranes are central elements of all eukaryotic and prokaryotic cells and provide the general structure of these cells. These membranes are mainly composed of lipids and proteins that are at the helm of many aspects of cellular function. The most fundamental component of all cellular membranes is a phospholipid, an amphiphilic molecule composed of a hydrophilic polar headgroup and a hydrophobic end tail. The hydrophobic tail with two fatty acid chains is attached to the hydrophilic head consisting of a glycerol-phosphate moiety topped with either an anionic, zwitterionic, or a cationic moiety. These phospholipids are commonly known as glycerophospholipids. When exposed to an aqueous environment, the phospholipids align in such a way that the hydrophobic tails orient against one another with the hydrophilic heads on either side facing the aqueous solution, thus spontaneously forming two layers or leaflets of what is known as the lipid bilayer.

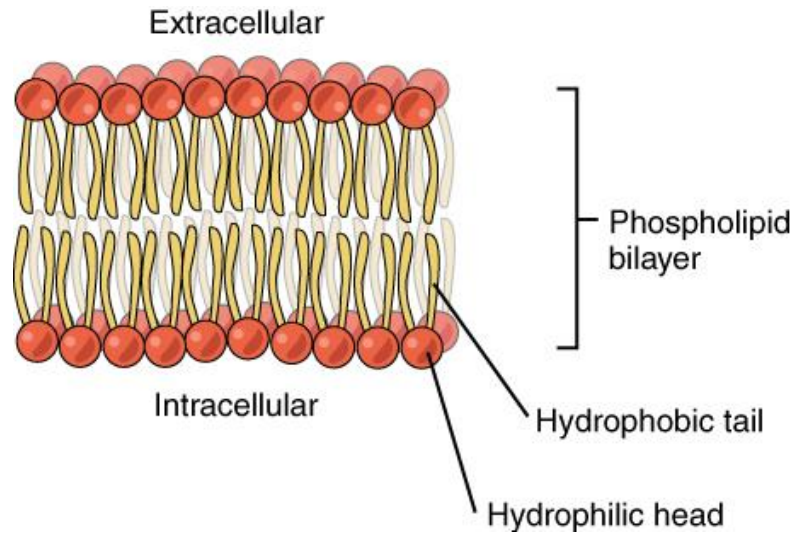


**Figure 1.02** Schematic structure of a phospholipid and lipid bilayer. [https://commons.wikimedia.org/wiki/File:0302\\_Phospholipid\\_Bilayer.jpg](https://commons.wikimedia.org/wiki/File:0302_Phospholipid_Bilayer.jpg)

Depending on molecular structure and environmental surroundings, the phospholipids have the ability to self-assemble into liposomes or vesicles. When water is introduced, the lipid bilayer will enclose an aqueous volume and create a structure similar to natural bilayer membranes due to the energetically favorable condition. Because of this inherent trait of lipid bilayers, these lipid systems are considered to be suitable models for the overall study of the cell membrane and its various properties, including dynamics, hydration, and electrostatics/surface potential.

### 1.2.2. Lipid Bilayers and Electrostatics

The lipid bilayers play a pivotal role in the cellular function of many cells, such as cell-to-cell signaling and transport of ions/compounds in and out of the cell. Many of these functions are thought to be the result of charges on the headgroups and associated potential from the diffuse double-layer. As mentioned above, the phospholipids can possess different charges on the headgroup. Figure 1.03 shows the conventional headgroups and their basic characteristics

found with glycerophospholipids. Some of the more commonly studied phospholipids are phosphatidylcholines, phosphatidylserines, and phosphatidylglycerol. Phosphatidylcholines (PC) are zwitterionic phospholipids that incorporate positively charged choline and negatively charged phosphate moieties. Phosphatidylserines (PS) are anionic phospholipids containing the amino acid serine at the hydroxyl end along with the negatively charged phosphate group. Phosphatidylglycerols (PG) are a class of anionic phospholipids that is comprised of a neutral glycerol and a negatively charged phosphate moiety.

Name of glycerophospholipid	Name of X	Formula of X	Net charge (at pH 7)
Phosphatidic acid	—	— H	-1
Phosphatidylethanolamine	Ethanolamine	— CH <sub>2</sub> —CH <sub>2</sub> —NH <sub>3</sub> <sup>+</sup>	0
Phosphatidylcholine	Choline	— CH <sub>2</sub> —CH <sub>2</sub> —N <sup>+</sup> (CH <sub>3</sub> ) <sub>3</sub>	0
Phosphatidylserine	Serine	— CH <sub>2</sub> —CH—NH <sub>3</sub> <sup>+</sup>   COO <sup>-</sup>	-1
Phosphatidylglycerol	Glycerol	— CH <sub>2</sub> —CH—CH <sub>2</sub> —OH   OH	-1
Phosphatidylinositol 4,5-bisphosphate	<i>myo</i> -Inositol 4,5-bisphosphate		-4
Cardiolipin	Phosphatidyl-glycerol	— CH <sub>2</sub>   CHOH   CH <sub>2</sub> —O—P(=O)(O <sup>-</sup> )—O—CH <sub>2</sub>   CH—O—C(=O)—R <sup>1</sup>   CH <sub>2</sub> —O—C(=O)—R <sup>2</sup>	-2

**Figure 1.03** Common headgroups found in glycerophospholipids and their basic characteristics.

[https://phys.libretexts.org/Courses/University\\_of\\_California\\_Davis/UCD%3A\\_Biophysics\\_241\\_-\\_Membrane\\_Biology/01%3A\\_Lipids/1.02%3A\\_Lipid\\_Headgroup\\_Types](https://phys.libretexts.org/Courses/University_of_California_Davis/UCD%3A_Biophysics_241_-_Membrane_Biology/01%3A_Lipids/1.02%3A_Lipid_Headgroup_Types)

Substituting the choline moiety with another functional group modifies the charge on the surface of the lipid bilayer. Since these charged headgroups are located at the surface of the bilayer, the overall polarity of the lipids is affected (a dipole formed from polar headgroups and nonpolar tails) and generates an electric field. As a result, the electrostatic environment

within the lipid bilayer and at the surface are quite different, thus, resulting in an electrostatic potential across the bilayer, as shown in Figure 1.04 [17].

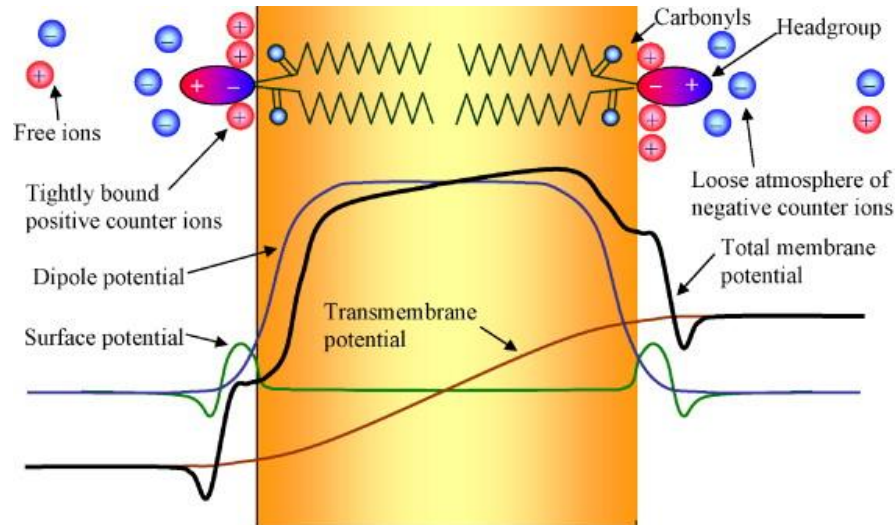


**Figure 1.04** Schematic representation of the electrostatic potential across a lipid bilayer due to charged groups at the interface. The three major components are displayed: dipole potential, transmembrane potential, and surface potential. Reproduced from ref. [17].

Three major components contribute to the electrostatic potential of the lipid bilayer membrane: the dipole potential, the transmembrane potential, and the surface potential. The dipole potential,  $\Psi_d$ , arises from the dipole moment created by the alignment of the hydrated phospholipids since it has a considerably weak dependence on the ionic composition of the surrounding medium. It is the strongest component of the membrane electrostatics. With the dipole potentials formed by the two monolayers of opposite electric charges, the combination of these oppositely charged layers creates a strong virtual positive charge in the center of the bilayer. The transmembrane potential,  $\Psi_t$ , is the net potential gradient produced by the ions and charges in the aqueous phases separated by the membrane. The  $\Psi_t$  is generally negative in value and an order of magnitude smaller than  $\Psi_d$ . The surface potential,  $\Psi_s$ , results from the combination of charges, including charges on the lipid headgroups, absorbed ions, and the

counter ions, located closely in the surrounding area of the headgroups on either side of the membrane at the lipid-water interface. Therefore, this potential is determined by the quantities and type of the charged phospholipids in the bilayer and the concentration of ions near the surface of the bilayer. In this project, we are interested in the surface potential  $\Psi_s$ .

The majority of the electrostatic interactions occur close to the lipid bilayer membrane surface. Therefore, these properties are profoundly significant to specific cellular functions of the bilayer and directly associated with any reactions between the membrane and ions, other small molecules, and charged residues of peripheral proteins in the immediate vicinity [18-20]. For this reason, it becomes imperative that experimental methods capable of accurately evaluating the membrane potential at such well-defined positions around or near the surface of the bilayer-water interface are developed to provide a comprehensive understanding of the membrane electrostatics and further decipher the mechanisms of biological phenomena in cells overall.

### **1.2.3. Substrate-supported Lipid Bilayers**

Liposomes prepared from synthetic lipids are frequently utilized as versatile models of cellular membranes to offer insight about the critical biological processes that normally occur in living organisms [21-24]. Despite their wide range of uses, problems often arise due to size dispersion and physical/chemical stability of the liposomes. One method to address some of these challenges is by having a substrate-supported lipid bilayer (SSLB) (example shown in Figure 1.05), which consists of anchoring the liposomes to a solid planar or spherical substrate [25-27]. In recent years, SLBs have become a popular and readily accessible technique for investigating the surface chemistry and sensitivity of the cell [28]. Moreover, the SLBs offer

insight into the interfacial electrostatic interactions in more detailed models of cellular membranes (which, for example, include integral molecules and account for nanoscale curvature effects) [29]. However, some of these SLBs, e.g., planar SLBs, are limited to a relatively narrow class of lipids and lipid-like molecules and have several other restrictions, such as temperature, pH, ionic strength, etc. Therefore, further experimental and theoretical efforts on SLBs are necessary to provide an excellent bilayer model system and allow for bilayer surface-sensitive investigations.

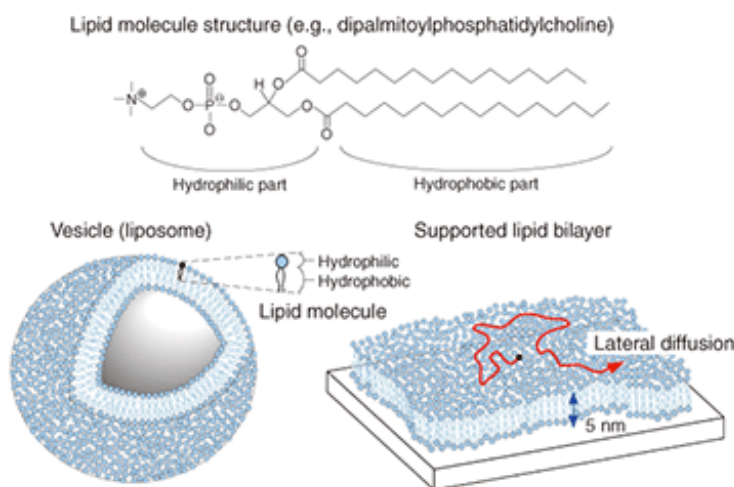


**Figure 1.05** Schematic representation of a substrate-supported lipid bilayer (SSLB). Reproduced from ref. [26].

More recently, nanoporous anodic aluminum oxide (AAO) substrates have been explored for SSLB studies, albeit using a different principle: while traditional SSLB rely on chemical and/or physical interactions with the substrate to keep the lipid bilayer attached, the rigid pores of AAO mechanically prevent the lipids from an expansion by confining them. As mentioned above, the AAO membranes are a robust inorganic material with macroscopically ordered, homogeneous nanopores with tunable diameter from ca. 20 to 200-400 nm. Thus, the diameter of the AAO pores controls the diameter of the SSLB. Additionally, these AAO substrates help

to preserve the vital membrane functions while simultaneously offering a wide range of opportunities to 1) steadily regulate pH and temperature, 2) adjust the composition of the bilayer, and 3) permit specific compounds/proteins into and out of the supported bilayer membrane [30]. This is due to their ability to promote the self-assembly of lipid nanotubular bilayers inside the pores and enhance membrane stability of the confined lipid bilayer. Furthermore, the AAO SSLBs grant more freedom to work with different spectroscopy techniques [24,27,31]. For this project, the technique of focus is magnetic resonance spectroscopy.

Magnetic resonance methods are known to offer a wealth of data on the structure of the SSLB systems. The macroscopic alignment of the lipid assemblies provided by the AAO structures assists in characterizing the biophysical properties of nanopore-confined molecules by magnetic resonance methods such as NMR and EPR. By utilizing modern magnetic resonance approaches, more insight can be gained into the macromolecular dynamics of the membrane lipids/proteins and, therefore, elucidate the potential for biotechnological and drug development applications.

### **1.3. Electron Paramagnetic Resonance Spectroscopy**

#### **1.3.1. Classical and Quantum Mechanical Description of EPR Spectroscopy**

Electron paramagnetic resonance (EPR) spectroscopy has been used to study the local molecular and electronic structure as well as molecular dynamics involving paramagnetic species. EPR spectroscopy is a powerful tool for investigating and detecting the magnetic

susceptibility associated with unpaired electrons in chemical species. Similar to nuclear magnetic resonance (NMR) spectroscopy, the underlying physics of EPR is fundamentally based on quantum mechanics. While NMR is based on a detection of transitions between nuclear spin states when placed in an external magnetic field, EPR is attributed to unpaired electron spins in an atom or molecule.

For a free electron, its interaction with an externally applied magnetic field directed along the z-axis is described by the following spin Hamiltonian operator,  $\hat{H}$ :

$$\hat{H} = -\hat{\mu}B_0 = -g_e\beta_e\hat{S}_zB_0 \quad (1.10)$$

where  $g_e$  is the g-factor for the free electron (2.00232),  $\beta_e$  is the electron Bohr magneton ( $9.27401 \times 10^{-24} \text{ JT}^{-1}$ ) and  $\hat{S}_z$  is the operator corresponding to the z-projection of the electron spin. The eigenvalues of the spin operator  $\hat{S}_z$  are  $m_s\hbar$ , with  $m_s = \pm \frac{1}{2}$ , and make up the components of the spin angular momentum along the z-axis direction. A simpler, more common notation uses the symbol  $\alpha$  for the  $m_s = +\frac{1}{2}$  state and  $\beta$  for the  $m_s = -\frac{1}{2}$  state. Therefore, when the field is present, a free electron will have two split energy states: the  $\alpha$  state increases in energy by  $\frac{1}{2}g_e\beta_eB_0$ , while the  $\beta$  state decreases by  $-\frac{1}{2}g_e\beta_eB_0$ . These two energy states of the free electron are generally referred to as Zeeman energy levels. In EPR spectroscopy, resonant absorption of electromagnetic (microwave) radiation between the two Zeeman energies occurs when the frequency of the microwave irradiation matches the resonant condition for energy-level separation,  $\Delta E$  (Figure 1.06).

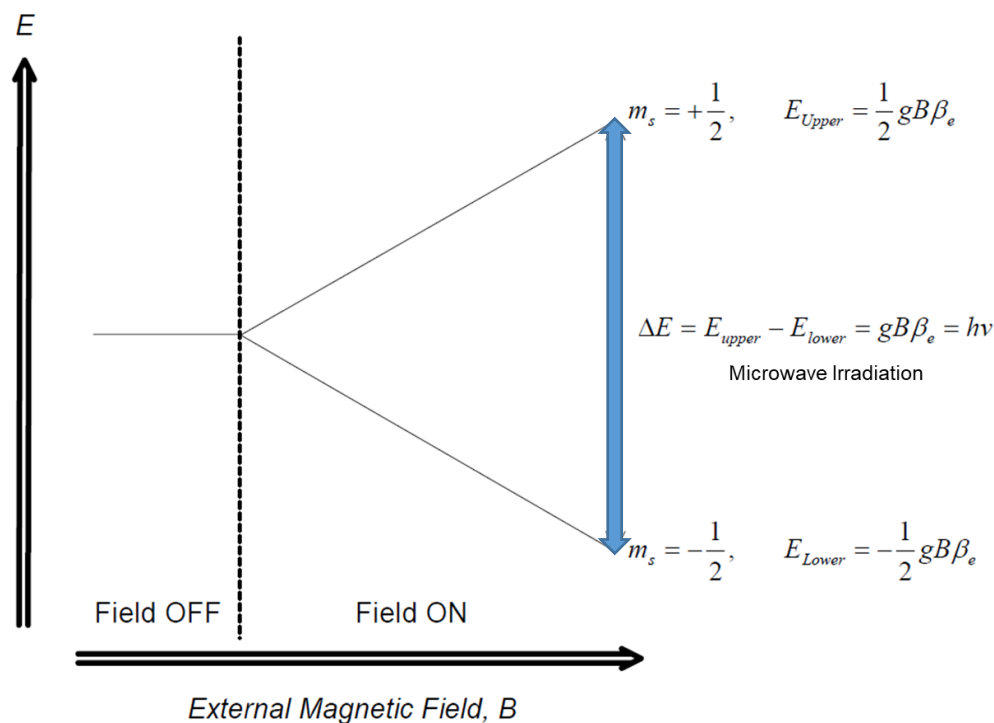


**Figure 1.06** Zeeman energy level of a free electron ( $S = \frac{1}{2}$ ) placed in a magnetic field. The blue arrow indicates the energy of the microwave quantum matching the energy splitting between the electron spin substates. Adapted from ref. [32].

Along with the Zeeman effect, there are additional interactions magnetic in nature (e.g., hyperfine coupling, dipolar coupling, zero-field splitting, etc.) that induce shifts or splitting of the Zeeman energy levels described by additional factors in the Hamiltonian operator. Within biophysical chemistry, these supplementary interactions are significant as they offer insight into the molecular geometry, electronic structure, and local molecular dynamics and interactions between spin systems and the local environment of the paramagnetic species.

### 1.3.2. Hyperfine Interaction

In addition to Zeeman interactions for paramagnetic species, the electron spins of these molecules can experience slight changes in energy-dependent upon the spin states of nuclei in the local environment. In the presence of a magnetic nucleus (such as  $^1\text{H}$  and  $^{14}\text{N}$ ), the spin of

the unpaired electron couples to the magnetic nucleus spin,  $I$ . This coupling induces further energy splitting of each electron Zeeman energy level. The size of this additional splitting is determined by the coupling constant,  $A$ . This electron-nuclear coupling is known as the hyperfine interaction. The selection rules for the electron spin transitions are  $\Delta m_s = 1$  and  $\Delta m_l = 0$ , since the microwave radiation induces electronic transitions but forbids nuclear transitions. At low magnetic fields (typically  $< 1$  T) the nuclear Zeeman interaction can be neglected and the energy of the observable EPR transitions can be approximated by the following expression:

$$\Delta E = h\nu = g_{iso}\beta_e B_0 + \sum_i A_i m_{I_i} \quad (1.11)$$

where  $g_{iso}$  is the isotropic g-factor for an electron spin,  $A_i$  is the hyperfine coupling constant to the nuclei denoted by  $i$ , and  $m_{I_i}$  is the z-axis projection of its spin  $I$ . The resulting spectrum has peaks that are centered at  $B_0 = \frac{h\nu}{g_{iso}\beta_e}$ . Because  $m_l = -I, -I + 1, \dots, 0, \dots, I - 1, I$ , each nuclear interaction results in  $2I + 1$  sub-states. For a collection of  $n$  equivalent nuclei, the result is  $2nI + 1$  sub-states with the total number of sub-states being the product of all the equivalent nuclei sub-states,  $n_{total} = \prod_i (2n_i I_i + 1)$ .

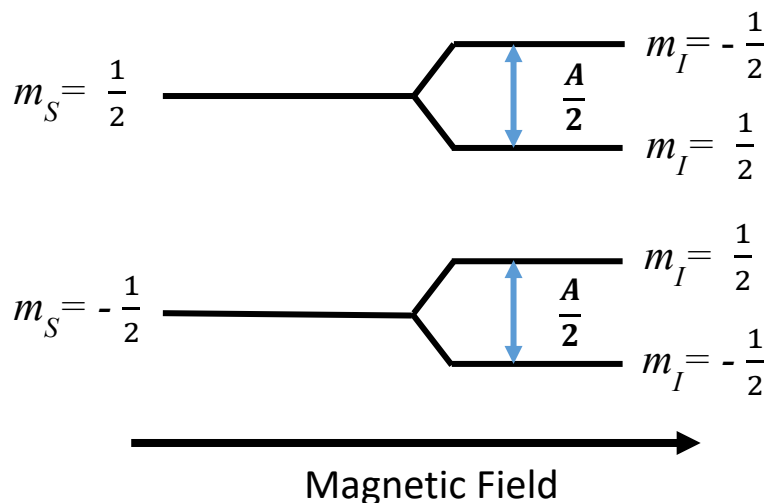


**Figure 1.07** Hyperfine splitting of a system consisting of an electron ( $S=1/2$ ) coupled to a nucleus ( $I=1/2$ ) with a coupling constant,  $A$ . Nuclear Zeeman interaction was neglected for simplicity.

The hyperfine interaction encompasses a Fermi contact term corresponding to the isotropic component of the interaction (independent of sample orientation with respect to the magnetic field) schematically shown in Figure 1.08A and a dipole-dipole term corresponding to the anisotropic component of the interaction (dependent on the sample orientation with respect to the magnetic field) shown in the Figure 1.08B.

The magnitude of the Fermi contact term is directly proportional to the electron spin density at the nucleus  $[\Psi(r)]^2$ . The size of the isotropic term provides information about the electronic structure of a paramagnetic center, such as covalent versus non-covalent bonding of a nucleus to the paramagnetic center. In liquid solutions, rapid tumbling of molecules effectively averages the dipolar term to zero. Therefore, the only contribution to the EPR spectrum is from the isotropic hyperfine component. However, biological samples generally fall within a slow-motion regime; thus, both the Fermi contact and dipolar interactions affect the spectra. The

anisotropic dipolar interaction is usually dominant in frozen solutions or solid powder samples, where no averaging effect occurs. The dipole-dipole interaction between the magnetic moments depends on the distance between the magnetic moments and the orientation of the spins. For the given distance  $r$  between the unpaired electron and nucleus and fixed angle  $\theta$  between the direction of the magnetic field and the vector connecting the electron to the nucleus, the dipolar interaction,  $D$ , is given by:

$$D \approx \frac{1-3\cos^2\theta}{r^3} \quad (1.12)$$

The anisotropic hyperfine interaction is an anisotropic through-space dipolar interaction that offers information on the distance, geometry, and location of the interacting spin species.

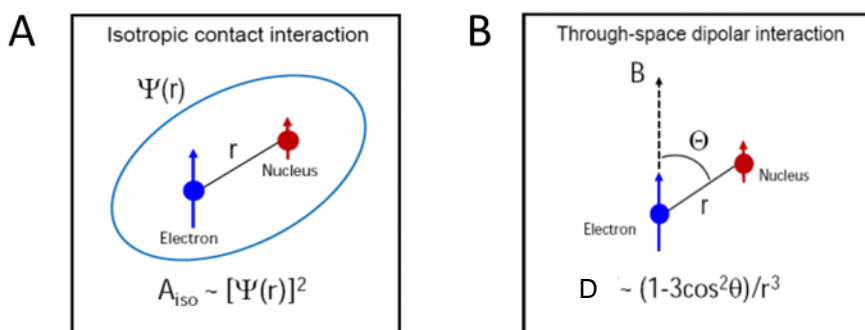


**Figure 1.08** Schematic descriptions of (A) isotropic coupling constant and (B) anisotropic hyperfine coupling constant.

### 1.3.3. Site-Directed Spin-labeling EPR

Site-directed spin-labeling (SDSL) in conjunction with EPR spectroscopy has emerged as a versatile and informative biophysical tool for elucidating structural and dynamic properties of biomacromolecules. Many biological systems, such as lipid membranes, are EPR silent (at least at room temperature) but can be studied upon introducing an EPR-active molecule called spin-label or a spin probe. SDSL is a variant of spin labeling EPR that is based on a covalent

attachment of a paramagnetic moiety – typically a stable organic radical such as nitroxide - to a specific site of a biomolecule (protein, nucleic acid, or lipid) and analysis of EPR spectra from such a label to obtain site-directed local data on the system structure and dynamics. Because of the small size of typical spin-labeled sidechain – with molecular volume comparable to that of phenylalanine- the labeling causes a little, if any, perturbation to the system. The SDSL method can be applied to opaque samples that are otherwise difficult to study optically, such as nanoporous substrates studied in this project [33-34].

In this project, we utilized nitroxide radicals with small molecular volumes that were covalently attached via disulfide bonds to the sulfhydryl groups of headgroup-modified lipids. The nitroxide possesses an electronic spin that is delocalized primarily over the N-O group. While the most abundant  $^{16}\text{O}$  has no nuclear spin, the abundant  $^{14}\text{N}$  has nuclear spin  $I=1$  (with projection quantum number  $m_I = -1, 0, 1$ ) and interacts with the electronic spin  $S=1/2$ . The resulting hyperfine interaction produces changes in the electronic spin energy levels (the last term on the right side of Equation 1.11 and causes splitting of the EPR energy levels into three sublevels corresponding to the different projection states of  $^{14}\text{N}$  nuclei. An example of this splitting for a nitroxide radical is given in Figure 1.09.

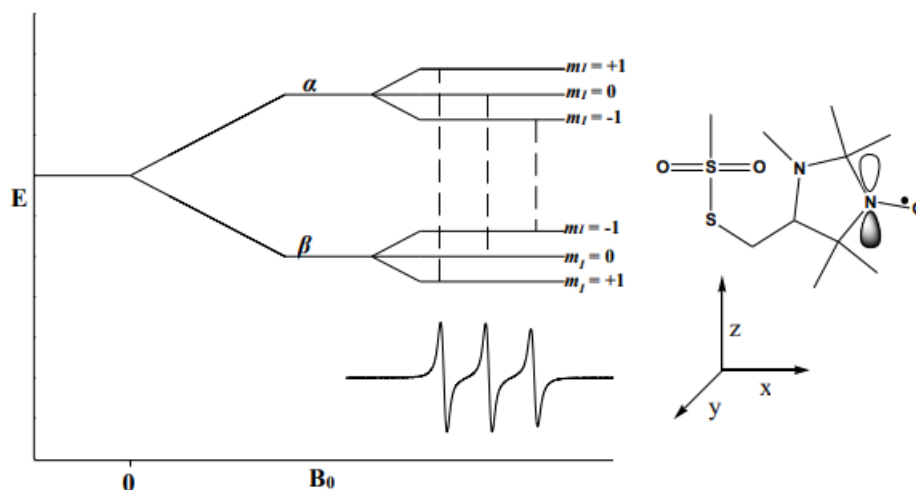


**Figure 1.09** Chemical structure of the nitroxide headgroup of IMTSL spin label and its EPR spectrum with three absorption peaks. Each energy level splits in three levels, and resonance frequency gives rise to three lines in X-band EPR. Reproduced from ref. [35].

The EPR spectra of nitroxides are sensitive to the rotational motion of the radical molecules. Therefore, they can be analyzed to derive rotational correlation time  $\tau_c$ , which roughly corresponds to the time for a spin label to rotate through an angle of a radian. Typical rotational correlation times of lipids and spin-labeled sidechains of proteins and peptides fall into 0.1 to 10 ns and can be measured from continuous wave (CW) EPR spectra. As rotational motion of the radical becomes slower (longer  $\tau_c$ ), the EPR spectra broaden, as shown in Figure 1.10.

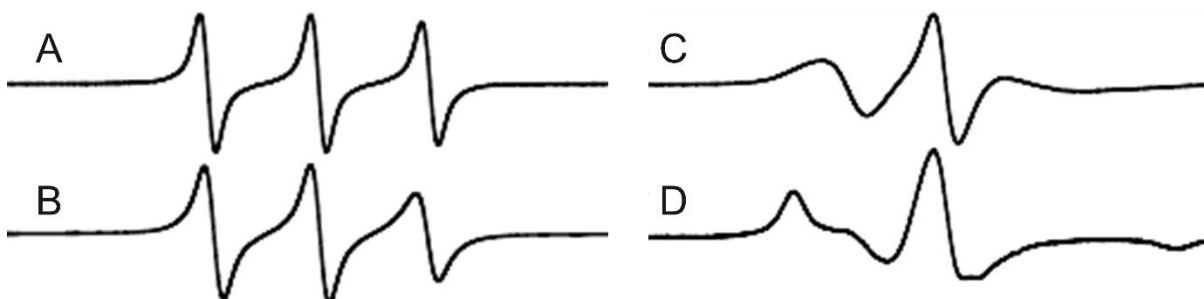


**Figure 1.10** EPR line shape as a function of spin label motion. (A) Spin label in dilute solution – fast motion. (B) Spin label attached to a small peptide in solution. (C) Spin-labeled peptide incorporated into a liposome – slow motion. (D) Fully protonated spin label within a liposome, experiencing electrostatic attraction to the bilayer surface. Adapted from ref. [35].

#### **1.4. Summary of Present Research**

The primary objectives of this research project were (1) to advance nanoporous AAO fabrication methods by optimization of pulse anodization techniques and exploring different pore surface modification methods with the goals of making such nanostructures conductive or semiconductive and (2) to investigate how surface electrostatic properties of nanotubular lipid bilayers confined in such nanopores are affected by the AAO fabrication procedures and pore geometry. For the latter, spin-labeling EPR of pH-sensitive stable nitroxide radicals was employed.

Using improved anodization methods in  $\text{H}_3\text{PO}_4$ , we present the results of enhanced fabrication of AAO by mild anodization and pulse anodization to produce larger uniformly ordered nanopores of diameter  $d \approx 450$  nm. Such large pores are viewed to be an essential step for incorporating large membrane protein complexes such as Photosystem I and Photosystem II.

Electroless deposition of conductive material (Au, carbon char, and ITO) into the AAO was also investigated as the means to promote conductivity of the AAO substrate. It was determined that there was insufficient deposition of the materials within the nanopores, which resulted in no conductivity. Although the electroless deposition did not yield desired results, electroless deposition of conductive materials through chemical processes is still of interest as a potential application for template-based study with conductivity, as the resulting advanced membranes could be used to offer more insight into the interactions between the nanoporous membranes and biomolecules for surface electrostatic studies of nanopore-confined biomolecules.

Finally, we employed spin-labeling EPR and pH-sensitive nitroxide radicals to assess the surface electrostatics of lipid bilayers through substrate-supported self-assembly within the AAO nanopores. A pH-sensitive headgroup labeled phospholipid probe (IMTSL-PTE) synthesized at NCSU was fully integrated into the lipid bilayer. The lipids were deposited onto the substrate and formed cylindrical phospholipid nanotubes in the pores. EPR spectra of such membrane probe reported on its ionization state and, thus, local pH. These spectroscopic data aided in determining the local surface electrostatic potential of nanopore-confined bilayers. By utilizing magnetic resonance approaches, more insight can be gained into the macromolecular dynamics of membrane lipids/proteins.

## 1.5. References

1. Lee, W.; Kim, J. Gösele, U. *Spontaneous Current Oscillations during Hard Anodization of Aluminum under Potentiostatic Conditions*. *Advanced functional materials*, 2010. **20**: 21-27.
2. Lee, W.; Ji, R.; Gösele, U.; Nielsch, K., *Fast fabrication of long-range ordered porous alumina membranes by hard anodization*. *Nature materials*, 2006. **5**: 741-747.
3. Lee, W.; Park, S., *Porous Anodic Aluminum Oxide: Anodization and Templated Synthesis of Functional Nanostructures*. *Chemical reviews*, 2014. **114**: 7487-7556.
4. Lu, C.; Chen, Z. *Anodic Aluminum Oxide—Based Nanostructures & Devices*. *Encyclopedia of nanoscience and nanotechnology*, 2011. **11**: 235-259.
5. Masuda, H.; Fukuda, K. *Ordered Metal Nanohole Arrays Made by a Two-Step Replication of Honeycomb Structures of Anodic Alumina*. *Science*, 1995. **268**: 1466-1468.
6. Lee, W.; et al. *Structural engineering of nanoporous anodic aluminium oxide by pulse anodization of aluminium*. *Nature nanotechnology*, 2008. **3**: 234-239.
7. Gun'ko, Y. K.; et al. *Chemical modification of silicon surfaces with ferrocene functionalities*. *Physica status solidi. A, Applied research*, 2003. **197**: 492-496.
8. Tanvir, S.; Pantigny, J.; Boulnois, P.; Pulvin, S. *Covalent immobilization of recombinant human cytochrome CYP2E1 and glucose-6-phosphate dehydrogenase in alumina membrane for drug screening applications*. *Journal of membrane science*, 2009. **329**: 85-90.
9. Routkevitch, D.; Bigioni, T.; Moskovits, M.; Xu, J. M. *Electrochemical Fabrication of CdS Nanowire Arrays in Porous Anodic Aluminum Oxide Templates*. *Journal of physical chemistry*, 1996. **100**: 14037-14047.
10. Liu, R.; Duay, J.; Lee, S. B. *Electrochemical Formation Mechanism for the Controlled Synthesis of Heterogeneous MnO<sub>2</sub>/Poly(3,4-ethylenedioxythiophene) Nanowires*. *ACS nanotechnology*, 2011. **5**: 5608-5619.
11. Kohli, P., Wharton, J.E., Braide, O., Martin, C. R. *Template Synthesis of Gold Nanotubes in an Anodic Alumina Membrane*. *Journal of nanoscience and nanotechnology*, 2004. **4**: 605-610.
12. Boyer, S. J.; Clarkson, R. B. *Electron paramagnetic resonance studies of an active carbon: The influence of preparation procedure on the oxygen response of the linewidth*. *Colloids and surfaces. A, physicochemical and engineering aspects*, 1994. **82**: 217-224.

13. Boehme, M.; Ionescu, E.; Fu, G.; Ensinger, W. *Room temperature synthesis of indium tin oxide nanotubes with high precision wall thickness by electroless deposition*. Beilstein journal of nanotechnology, 2011. **2**: 119-126.
14. Elam, J. W.; Routkevitch, D.; Mardilovich, P. P.; George, S. M. *Conformal Coating on Ultrahigh-Aspect-Ratio Nanopores of Anodic Alumina by Atomic Layer Deposition*. Chemistry of materials, 2003. **15**: 3507-3517.
15. Fang, M.; Ho, J. C. *Area-Selective Atomic Layer Deposition: Conformal Coating, Subnanometer Thickness Control, and Smart Positioning*. ACS nanotechnology, 1900. **9**: 8651-8654.
16. Jani, A. M. M.; Losic, D.; Voelcker, N. H. *Nanoporous Anodic Aluminium Oxide: Advances in Surface Engineering and Emerging Applications*. Progress in Materials Science, 2013. **58**: 636–704.
17. Demchenko, A. P.; Yesylevskyy, S. O. *Nanoscopic description of biomembrane electrostatics: results of molecular dynamics simulations and fluorescence probing*. Chemistry and Physics of Lipids 2009. **160**(2): 63-84.
18. Gurtovenko, A. A., Vattulainen I. *Calculation of the electrostatic potential of lipid bilayers from molecular dynamics simulations: Methodological issues*. Journal of chemical physics, 2009. **130**: 215107.
19. Cevc, G. *Membrane electrostatics*. Biochimica et Biophysica Acta. 1990. **1031**: 311–382.
20. Voinov, M. A., Rivera-Rivera, I., Smirnov, A. I. *Surface Electrostatics of Lipid Bilayers by EPR of a pH-Sensitive Spin-Labeled Lipid*. Biophysical journal. 2013. **104**(1): 106-116.
21. Jones, M.N., *The surface properties of phospholipid liposome systems and their characterisation*. Advances in colloid and interface science, 1995. **54**: 93-128.
22. Nielsen, L.K., et al., *Lag-burst kinetics in phospholipase A 2 hydrolysis of DPPC bilayers visualized by atomic force microscopy*. Biochimica et biophysica acta (BBA)-biomembranes, 1999. **1420**(1): 266-271.
23. Nagle, J.F. and S. Tristram-Nagle, *Structure of lipid bilayers*. Biochimica et biophysica acta (BBA)-reviews on biomembranes, 2000. **1469**(3): 159-195.
24. Mornet, S., et al., *The formation of supported lipid bilayers on silica nanoparticles revealed by cryoelectron microscopy*. Nano letters, 2005. **5**(2): 281-285.
25. Jackman, J. A., Cho, N-J. *Supported Lipid Bilayer Formation: Beyond Vesicle Fusion*. Langmuir, 2020, **36**(6): 1387–1400.
26. Furukawa, K. NTT Technical Review. 2022.

27. Sackmann, E., *Supported membranes: scientific and practical applications*. Science, 1996. **271**(5245): 43.
28. Castellana, E. T., Cremer, P. S. *Solid supported lipid bilayers: From biophysical studies to sensor design*. Surface Science Reports. 2009. **61**(10): 429-444.
29. Voinov, M. A., Kirilyuk, I. A., Smirnov, A. I., *Spin-Labeled pH-Sensitive Phospholipids for Interfacial pKa Determination: Synthesis and Characterization in Aqueous and Micellar Solutions*. Journal of physical chemistry B, 2009. **113**, 3453–3460.
30. Terrettaz, S., et al., *Immunosensing by a Synthetic Ligand-Gated Ion Channel*. Angewandte chemie international edition, 2001. **40**(9): 1740-1743.
31. Baksh, M.M., et al., *Neuronal activation by GPI-linked neuroligin-1 displayed in synthetic lipid bilayer membranes*. Langmuir, 2005. **21**(23): 10693-10698.
32. Alaouie, A. M., *Lipid Nanotube Arrays: Exploring Nanoscale Phenomena on Lipid-Substrate Interfaces*. 2006. <http://www.lib.ncsu.edu/resolver/1840.16/5482>
33. Mchaourab, H.S., et al., *Motion of spin-labeled side chains in T4 lysozyme. Correlation with protein structure and dynamics*. Biochemistry, 1996. **35**(24): 7692-7704.
34. Klug, C.S. and J.B. Feix, *Methods and applications of site-directed spin labeling EPR spectroscopy*. Methods in cell biology, 2008. **84**: 617-658.
35. Donohue, M.P., *On the Nature of Electrostatics at the Interface of Transmembrane Peptides and Lipid Bilayers*. 2014. <http://www.lib.ncsu.edu/resolver/1840.16/9953>

## CHAPTER 2: ENHANCED FABRICATION OF AAO

### 2.1. Introduction

Over the last two decades, nanoporous AAO has been of particular interest for research in many aspects of nanoscience and nanotechnology. Due to its cost-effective and simple electrochemical fabrication along with its appealing properties, it is one of the most widely used nanoporous materials for various nanotechnological applications [1-5]. Several innovations in advanced electronics [1-9], bioengineering [10-12], drug development [13-14], and catalysis [15-18] have been made with AAO.

Under optimal fabrication conditions, AAO consists of macroscopically ordered, hexagonally-packed homogeneous nanopores with tunable diameter ranging from ca. 20 to 400 nm. To fabricate the nanoporous AAO, Al undergoes a two-step anodization where the Al is oxidized in acidic electrolytes at an appropriate voltage. Specific characteristics of the AAO, e.g., pore diameter, interpore distance and thickness of the formed oxide layer (Figure 2.01), can be structurally engineered by the operating parameters like the electrolyte type, concentration, and temperature, relevant applied voltage, and duration of the second step of anodization [24-25] and by means of various anodization regimes, like mild or hard anodization. The three acidic electrolytes commonly used to form the AAO are sulfuric acid ( $\text{H}_2\text{SO}_4$ ), oxalic acid ( $\text{H}_2\text{C}_2\text{O}_4$ ), and phosphoric ( $\text{H}_3\text{PO}_4$ ) with their respective voltages of 25, 40, and 195 V.

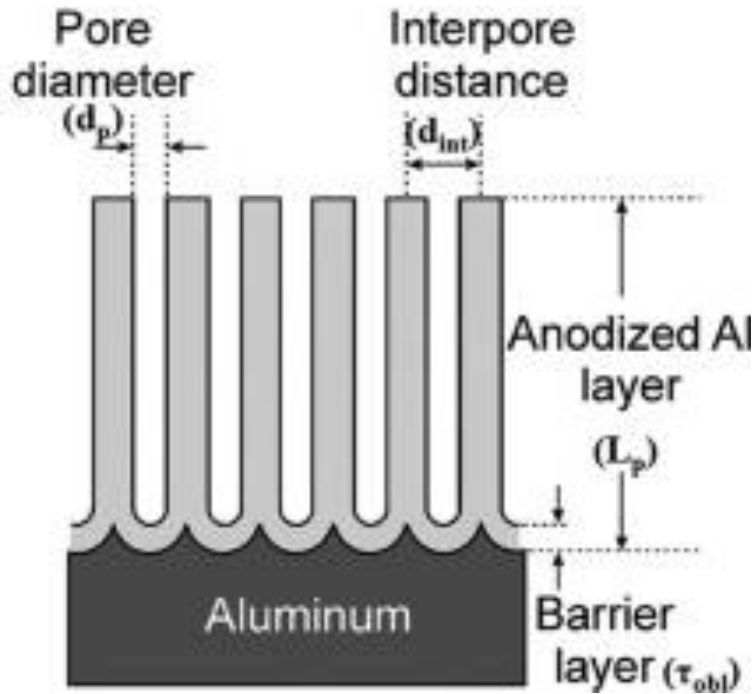


**Figure 2.01** Tunable AAO pore dimensions controlled by the anodization process. Reproduced from ref. [26]

Conventional anodization (or mild anodization, MA) is the most widely adopted way to carry out the anodization process. It involves a slow steady-state oxidation of the Al with pore growth at a rate of  $\sim 2 \mu\text{m h}^{-1}$ . Another anodization regime is hard anodization (HA), which speeds up the anodization substantially (pore growth rate  $\sim 50\text{-}100 \mu\text{m h}^{-1}$ ) [27]. However, the resulting nanopores are typically less ordered, and the high-speed anodization may cause the oxide layer to overheat and burn. To address these deficiencies, a pulse anodization (PA) process has been introduced, in which the voltage is continuously modulated with short voltage pulses of anodization and longer rests in between [24]. This pulse regime aids in dispersing some of the accumulated heat but still does not permit full control of the pore ordering. In more recent years, many of these anodization approaches have been intensively explored to fabricate better

AAO nanostructured materials in a shorter fabrication time and to improve upon their unique pore properties, mainly to generate larger nanopores (<200 nm).

In this chapter, we investigated the use of improved anodization methods to produce larger uniformly ordered nanopores. The results of enhanced fabrication of AAO by mild anodization and by pulse anodization at a slightly lower voltage using  $\text{H}_3\text{PO}_4$  as the electrolyte are presented. At this slightly lower voltage, some of the heat accumulated from the high-speed growth is expected to decrease during MA and disperse during the rest periods of PA. These larger nanopores are significant for our study due to their potential use as a substrate-support for macroscopic lipid bilayer systems.

## **2.2. Experimental Section**

### **2.2.1. Materials and Chemicals**

All chemicals of the ACS Reagent grade or higher were purchased from Sigma Aldrich/Merck, KGaA (Darmstadt, Germany) or VWR International, LLC (Radnor, PA, USA) unless otherwise indicated.

### **2.2.2. Mild Anodization of Aluminum in Phosphoric Acid**

The MA AAO samples were prepared by subsequent anodization steps involving a first and second anodization, aluminum metal removal, and pore enlargement through etching. A high-purity aluminum foil (99.99%, 0.127 mm thick, Strem Chemicals, Inc., Newburyport, MA, USA) was utilized as the starting material. An initial mild anodization step was carried out at

40 V in 4 wt%  $\text{H}_2\text{C}_2\text{O}_4$  for 5-7 h for all the samples. The backside of the foil was masked by clear nail polish (Electron Microscopy Sciences, Hatfield, PA, USA). Immediately after that, the second anodization step was started. The front side of the foil underwent mild anodization at 189 V in  $\text{H}_3\text{PO}_4$  for 16 h. After the anodization process, the nail polish protective layer was removed by rinsing the sample with acetone. A thin aluminum oxide layer formed underneath the protective layer by the first anodization was removed by floating the anodized pieces on the surface of 10 vol%  $\text{H}_3\text{PO}_4$  solution for about 3 h. The remaining metallic aluminum was dissolved in 10 wt%  $\text{CuCl}_2$  solution at room temperature under mild sonication. To open the nanopores of the back end of the samples obstructed by the barrier oxide layer, the pieces were treated (floated barrier down) with 10 vol%  $\text{H}_3\text{PO}_4$  solution until moisture was spotted on the top, indicating the opening of the nanopores. Subsequently, the pore diameter was enlarged by etching the samples in 5 vol%  $\text{H}_3\text{PO}_4$  for 3 and 7 h. The samples were thoroughly rinsed with deionized water and air-dried to complete the process.

The pore morphology and structure of all the fabricated AAO were examined by FEI Verios 460L SEM instrument installed and operated by the NCSU Analytical Instrumentation Facility (AIF). For SEM imaging, small pieces of AAO were broken from the larger membranes and mounted on a sample holder using double-sided carbon tape (Electron Microscopy Sciences). Low accelerating potentials (e.g., 500 V) were employed to suppress sample charging. The pore diameters were analyzed directly from the SEM images using ImageJ (NIH) software.

### **2.2.3. Pulse Anodization of Aluminum in Phosphoric Acid**

The PA AAO samples were prepared by subsequent anodization steps involving a first and second anodization, aluminum metal removal, and pore enlargement through etching. A high purity aluminum foil (99.99%, 0.127 mm thick, Strem Chemicals, Inc., Newburyport, MA, USA) was utilized as the starting material. The foil was annealed at 520 °C and put into a holder provided by Dr. Antonin Marek (NCSU). Teflon tape was wrapped around the holder's inner grips to prevent the electrolyte solution from seeping inside. An initial pulse anodization step was carried out with a ramp from 100-189 V, rest at 170V, 5 s on, 30 s off, and a current threshold at 0.185 A in H<sub>3</sub>PO<sub>4</sub> for 14 h for all the samples. The backside of the foil was masked by clear nail polish (Electron Microscopy Sciences, Hatfield, PA, USA). Immediately after that, the front side of the foil underwent pulse anodization with a ramp from 150-189 V with rest at 170V, 5s on, 15s off, and a current threshold at 170e-3 A in H<sub>3</sub>PO<sub>4</sub> for 20 h. To complete the anodization process, a final pulse anodization occurred with continuous anodization at 189 V and a current threshold at 80e-3 A for 18 h. After the anodization process, the nail polish protective layer was removed by rinsing the sample with acetone. An aluminum oxide layer formed underneath the protective layer by the first anodization was removed by floating the anodized pieces on the surface of 10 vol% H<sub>3</sub>PO<sub>4</sub> solution for about 3 h. The remaining metallic aluminum was dissolved in 10 wt% CuCl<sub>2</sub> solution at room temperature under mild sonication. To open the nanopores of the back end of the samples obstructed by the barrier oxide layer, the pieces were treated (floated barrier down) with 10 vol% H<sub>3</sub>PO<sub>4</sub> solution at 45 °C until moisture was spotted on the top, indicating an opening of the nanopores.

The pore morphology and structure of all the fabricated AAO were examined by FEI Verios 460L SEM instrument installed and operated by the NCSU Analytical Instrumentation Facility (AIF). For SEM imaging, small pieces of AAO were broken from the larger membranes and mounted on a sample holder using double-sided carbon tape (Electron Microscopy Sciences). Low accelerating potentials (e.g., 500 V) were employed to suppress sample charging.

## **2.3. Results and Discussion**

### **2.3.1. AAO Fabrication with Mild Anodization in Phosphoric Acid**

Figure 2.02 shows representative SEM images of the top (A-C) and bottom of the nanoporous AAO membranes (B-D) fabricated for this study. The images of the H<sub>3</sub>PO<sub>4</sub> AAO with 3 h etching (Figure 7A-B) exhibit a partial pore ordering on both sides of the membrane. The images of the H<sub>3</sub>PO<sub>4</sub> AAO with 7 h etching (Figure 7 C-D) display an improved pore regularity at high porosity with diameter  $d = 450 \pm 41$  nm on the bottom side. There is still a slight disordering on the top side of the membrane coming from etching the interface between the remnants of the first protective anodization step and the large pores of the second anodization step.

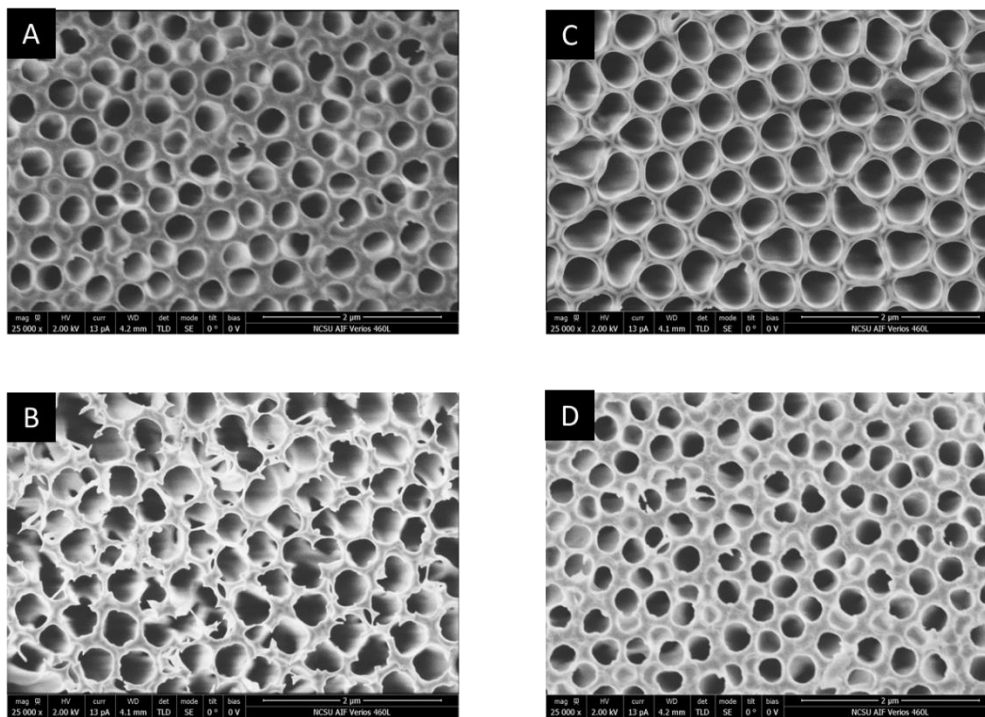


**Figure 2.02** SEM images of (A,C) top and (B,D) bottom sides of the AAO membranes fabricated by mild anodization in  $H_3PO_4$  at 189 V. (A-B) AAO membrane after 3 h of etching; (C-D) AAO membrane after 7 h etching.

A protective layer is produced to shield the AAO from burning. That is achieved by partially organizing the pores and by oxygen-limited diffusion, which regulate spikes in anodization current and heat development. However, to further improve the pore structure's hexagonal organization, it would be better to avoid using the protective layer. In that case, the full two-stage anodization procedure can be employed, e.g., with both steps at the same voltage regime, that is known to significantly improve the pore regularity. This method contrasts with the existing two-step process at two different voltage regimes—such a combined approach resulting in different anodized layers with varying pore morphology. The protective layer has a smaller interpore distance,  $\sim 100$  nm at 40 V, while the additional layer typically has much larger interpore distances,  $\sim 500$  nm at 200 V. The protective layer can be removed during

etching, but the transition interface region still becomes an issue. One promising way to eliminate the need for the protective layer is to utilize a pulse anodization regime, in which an alternating current is switched on and off to provide for a more efficient cooling of the anodized sample. With a more extended switched-off period, there is more controlled heat development during the switched-on period. Thus, the pulse anodization will decrease the burning of the AAO. As a downside, this approach comes at the cost of an extended period of anodization time needed to achieve a specific AAO thickness.

### **2.3.2. AAO Fabrication with Pulse Anodization in Phosphoric Acid**

The initial pulse anodization was adequate and consistent. However, during the second pulse anodization step, the anodized pieces started to burn at the edge in the holder or in random areas along the edges. Such a burning resulted in massive spikes in current and a visible dark discoloration of the AAO layer. The burning is due to electrolytic breakdown, which typically occurs with high current density conditions. Once the burning spots were detected, the burned spots were covered with nail polish, and the pulse regime was frequently continued. After a few hours of anodization, the electrolyte solution started to seep into the holder. This would cause the piece to continue burning or the electrolyte to anodize the metal clip holding the Al piece. To alleviate this problem, we decided to implement a supplemental MatLab script for the PA process to allow for the system to automatically sense when the current was starting to rise rapidly (meaning breakdown of the piece was either starting to happen or about to happen), which would reset/continue the process or immediately stop the PA regime. After implementing such a procedure, the Al pieces started to anodize for longer times. However, there was no consistency in the amount of anodization before a breakdown would completely

override the process. In addition, the anodization process would stop more frequently due to the detection of an increase in current, although little to no burning occurred. This was attributed to inherent stress of the Al that impacted the anodization and the manner in which the pores were formed [24]. Taking this into consideration, the Al was annealed at 520 °C to relieve the stress before anodization. This annealing improved the anodization process, allowing for a better second PA step.

After removing the Al metal, the barrier layer was etched in  $\text{H}_3\text{PO}_4$  to begin opening the pores from the back. Etching for more than 1 h at a higher temperature resulted in the piece being completely dissolved in the solution. This anodization scheme produced AAO with ~70-80  $\mu\text{m}$  thickness without further etching of the pores. However, there was severe pore disordering and irregularity, as seen in Figure 2.03. This pore disordering contrasts with previously fabricated AAO in the Smirnov group with more uniform pores. This is likely due to the different experimental parameters used to fabricate this AAO in  $\text{H}_3\text{PO}_4$ . Lastly, most of the AAO pieces were very brittle.

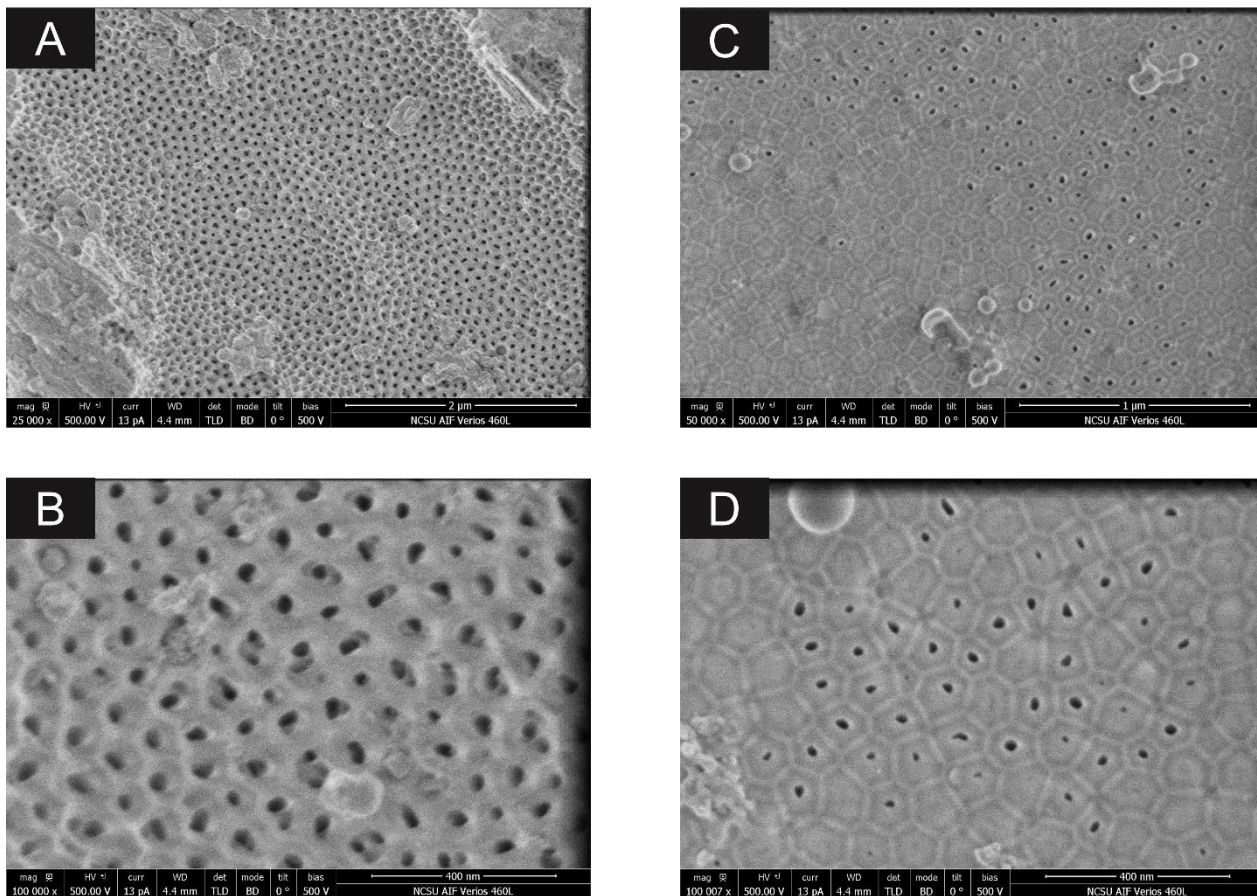


*Figure 2.03 SEM images of (A–B) top and (C–D) bottom sides of the AAO membranes fabricated by pulse anodization in  $H_3PO_4$  at 189 V.*

## 2.4. Conclusion

An enhanced anodization of the AAO based on a mild and a pulse anodization of aluminum in phosphoric acid at a lower potential to generate larger nanopores was investigated. While nanopores of a larger diameter ( $d=450 \pm 41$  nm) were successfully fabricated using mild anodization, the pores had a slight disordering resulting from the initial protective anodization step in oxalic acid. To improve the uniform ordering of the AAO, a pulse anodization regime was employed. The overall procedure for the pulse anodization was problematic because of an electrolytic breakdown and/or stress defects of the Al surface. The breakdown and stress issues were mitigated by automating the anodization process, using an additional Matlab script, and

annealing Al strips before the anodization to relieve the existing stress. Based on these improvements, AAO was successfully fabricated using the pulse regime. However, the AAO pieces were brittle and had severe pore irregularity.

The achieved results from both anodization methods indicate a further need to re-examine the anodization procedures to achieve larger nanopores with greater pore uniformity. In addition, the advanced AAO from the improved regime could bear significant implications for template synthesis or surface modification studies.

## 2.5. References

1. Föll, H.; et al. *Pores in III–V Semiconductors*. *Advanced materials*, 2003. **15**: 183-198.
2. Thompson, G. E. *Porous anodic alumina: fabrication, characterization and applications*. *Thin solid films*, 1997. **297**: 192-201.
3. Gusev, E. P.; et al. *High-resolution depth profiling in ultrathin Al<sub>2</sub>O<sub>3</sub> films on Si*. *Applied physical letters*, 2000. **76**: 176.
4. Jongsomjit, B.; Panpranot, J.; Goodwin Jr., J. G. *Co-Support Compound Formation in Alumina-Supported Cobalt Catalysts*. *Catalysis*, 2001. **204**(1): 98-109.
5. Peercy, P. S. *The drive to miniaturization*. *Nature*, 2000. **406**(6799): 1023-1026.
6. Mao, A.; et al. *Surface roughened 1-D Au host nanorods for visible light induced photocatalyst*. *Electrochimica Acta*, 2013. **97**: 404.
7. Kikuchi, T.; et al. *Fabrication of a meniscus microlens array made of anodic alumina by laser irradiation and electrochemical techniques*. *Electrochimica Acta*, 2013. **94**: 269.
8. Bocchetta, P.; Conciauro, F.; Santamaria, M.; Di Quarto, F. *Cs<sub>0.86</sub>(NH<sub>4</sub>)<sub>1.14</sub>SO<sub>4</sub>Te(OH)<sub>6</sub> in porous anodic alumina for micro fuel cell*, *Electrochimica Acta*, 2011. **56**: 3845.
9. Bocchetta, P.; Santamaria, M.; Di Quarto, F. *Preparation of Large Area Anodic Alumina Membranes and their Application to Thin Film Fuel Cell*. *Journal material science and nanotechnology*, 2014. **1**: S104.
10. Chen, J.; et al. *Performance of through-hole anodic aluminum oxide membrane as a separator for lithium-ion battery*, *Journal of membrane science*, 2014. **461**: 22.
11. Kumeria, T.; et al. *Nanoporous Anodic Alumina Rugate Filters for Sensing of Ionic Mercury: Toward Environmental Point-of-Analysis Systems*. *ACS applied material interfaces*, 2014. **6**: 12971.
12. Kumeria, T.; Santos, A.; Losic, D. *Nanoporous Anodic Alumina Platforms: Engineered Surface Chemistry and Structure for Optical Sensing Applications*. *Sensors*, 2014. **14**: 11878.
13. Królikowska, A.; *Surface-enhanced resonance Raman scattering (SERRS) as a tool for the studies of electron transfer proteins attached to biomimetic surfaces: Case of cytochrome C*, *Electrochimica Acta*, 2013. **111**: 952.
14. Das, G.; et al. *Fabrication of large-area ordered and reproducible nanostructures for SERS biosensor application*. *Analyst*, 2012. **137**: 1785.

16. Prida, V.M.; et al. *Electroplating and magnetostructural characterization of multisegmented Co<sub>54</sub>Ni<sub>46</sub>/Co<sub>85</sub>Ni<sub>15</sub> nanowires from single electrochemical bath in anodic alumina templates*, *Nanoscale research letters*, 2013. **8**: 1.
17. Ramazani, A.; et al. *A new approach to fabricating magnetic multilayer nanowires by modifying the ac pulse electrodeposition in a single bath*. *Journal of physical D: applied physics*, 2014. **47**: 355003.
18. Thorat, S.B.; Diaspro, A.; Salerno, M. *In vitro investigation of coupling-agent-free dental restorative composite based on nano-porous alumina fillers*, *Journal of dentistry*, 2014. **42**: 278.
19. Wang, Y.; et al. *Bioinert Anodic Alumina Nanotubes for Targeting of Endoplasmic Reticulum Stress and Autophagic Signaling: A Combinatorial Nanotube-Based Drug Delivery System for Enhancing Cancer Therapy*. *ACS Applied material interfaces*, 2015. **7**: 27140.
20. Rahman, S. et al. *Nanoengineered drug-releasing aluminium wire implants: comparative investigation of nanopores geometry, drug release and osteoblast cell adhesion*. *RSC advances*, 2015. **5**: 75004.
21. Kikuchi, T.; et al. *Fabrication of Self-Ordered Porous Alumina via Etidronic Acid Anodizing and Structural Color Generation from Submicrometer-Scale Dimple Array*. *Electrochimica Acta*, 2015. **156**: 235–243.
22. Chen, Y.; et al. *Biomimetic Nanoporous Anodic Alumina Distributed Bragg Reflectors in the Form of Films and Microsized Particles for Sensing Applications*. *ACS applied material interfaces*, 2015. **7**: 19816.
23. Takenaga, A.; et al. *Self-Ordered Aluminum Anodizing in Phosphonoacetic Acid and Its Structural Coloration*, *ECS solid state letters*, 2015. **4**: P55.
24. Kure-Chu, S.Z. et al. *Facile Fabrication of Ordered Multi-Tiered Hierarchical Porous Alumina Nanostructures with Multiple and Fractional Ratios of Pore Interval toward Multifunctional Nanomaterials*, *ECS journal of solid state science technology*, 2016. **5**: P285.
25. Lee, W.; Park, S., *Porous Anodic Aluminum Oxide: Anodization and Templated Synthesis of Functional Nanostructures*. *Chemical reviews*, 2014, **114**: 7487-7556.
26. Stepniowski, W.J.; et al., *The influence of electrolyte composition on the growth of nanoporous anodic alumina*. *Electrochimica Acta*, 2016, **211**: 453–460.
27. Balde, M.; Vena, A.; Sorli, B. *Fabrication of porous anodic aluminium oxide layers on paper for humidity sensors*. *Sensors and actuators B, chemical*, 2015. **220**: 829-839.

28. Losic, D., Lillo, M., Losic Jr, D. *Porous Alumina with Shaped Pore Geometries and Complex Pore Architectures Fabricated by Cyclic Anodization*. *Small*, 2009. **5**(12): 1392–1397.

## **CHAPTER 3: ELECTROLESS DEPOSITION INTO AAO SUBSTRATE FOR CONDUCTIVITY**

### **3.1. Introduction**

The fabrication of AAO membranes has been the focus of many current studies in regard to their potential theoretical and functional uses [1-4]. Of particular interest, the template method is a versatile and successful approach for the fabrication of nanostructures, e.g., nanoparticles, nanotubes, or nanowires, with AAO [5-7]. With this method, various types of nanomaterials have been obtained, such as metals [8-9], semiconductors [10], polymers [11-12], carbon [13], [14], and other materials. The major advantage of this method is the ability to fill the AAO nanopores with desired material to create the nanostructures or alter the electronic, mechanical, and chemical properties of the AAO membranes with convenient strategies.

In addition to being cost-effective, the AAO membranes allow for quick and easy applications without the need for state-of-the-art equipment [15-16]. One of these simpler applications is the electroless deposition of conductive substances, such as metals or metal oxides. The conductive substances are uniformly deposited within the nanopores and on the surface of the AAO membranes to modify the electrical properties of the membrane [17]. However, the AAO is an inert material, which negatively impacts the electroless deposition unless the AAO surface is initially primed. Subsequently, for this approach to occur, the membrane must first be activated with a metal (e.g., Ag, Pd, Sn) to aid in the deposition of a catalyst. After the activation and catalyst deposition, a reduction transpires, allowing for the chemical deposition of a conductive metal. As a result, the AAO membranes acquire conductive properties.

The work presented in this chapter aims to develop a modified electroless deposition strategy of AAO membranes using Au, carbon char, and indium tin oxide (ITO). For this purpose, the surface structure and electrical properties of the AAO membranes change, promoting their use as a semiconductor. Furthermore, these advanced membranes with conductive properties could be utilized as a biosensor to provide more information about the interaction between the nanoporous membranes and biomolecules and the surface properties of these nanopore-confined biomolecules.

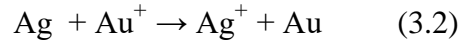
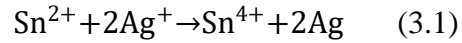
## **3.2. Experimental Section**

### **3.2.1. Materials and Chemicals**

All chemicals and solvents were purchased from VWR International (Radnor, PA, USA) or Fisher Scientific (Waltham, Massachusetts, USA) unless otherwise indicated and used without further purification. The commercial gold plating solution was purchased from Sigma-Aldrich (St. Louis, MO, USA). Commercial Anodic Aluminum Oxide (AAO) membranes were manufactured by Whatman (UK). The thickness of the AAO substrate was  $\sim 50$   $\mu\text{m}$ , and the nominal pore diameter was 200 nm. Anodic Aluminum Oxide (AAO) membranes were manufactured in the Smirnov group (NCSU). The thickness of the AAO was 72  $\mu\text{m}$ , and the pore diameter was 79 nm.

### 3.2.2. Electroless Deposition of Gold into AAO

The Au deposition process for the AAO templates was conducted using a slightly modified literature procedure by Kohli et al. [17]. The following redox reactions describe the chemistry behind the deposition process:



First, the AAO membranes were surface modified with a ligand containing succinic anhydride moiety using the following procedure. AAOs were incubated for 48 h in 0.1 M toluene solution of (3-triethoxysilyl)propylsuccinic anhydride (SAPT). To remove air and allow for the SAPT solution to diffuse into the AAO easily and freely, the incubating membrane was vacuumized for 1 min. After that, the membranes were washed in ethanol for 1 min and then in chloroform for 20 min at 60°C. The washing process was repeated twice to ensure the complete removal of the excess silane from AAO. Next, the succinic anhydride groups of the AAO-coated ligands were hydrolyzed with ultra-pure water for 1 h at 40°C to yield succinic acid residues. The purpose of these residues is to chelate  $\text{Sn}^{2+}$  at the AAO surface. The covalent attachment of the silane ligands to the membrane surface and hydrolysis of the ligands was confirmed by FT-IR analysis.

Further deposition steps were carried out to ensure that Au was deposited on the nanopore surface but not on the membrane surface. First, one of the AAO membrane faces was masked with a piece of an electrical tape. After that, the membrane was incubated for 45 min in an aqueous solution (activation solution) that contained 0.027 M  $\text{SnCl}_2$  and 0.07 M trifluoroacetic

acid (TFA). After the incubation, AAO was rinsed thoroughly with water, and the tape was carefully removed with ethyl acetate. Next, the membrane was allowed to dry in air at room temperature. After drying, the opposite face of the membrane was masked with a second piece of electrical tape, and then the membrane was submerged for 30 min in a catalytic solution comprised of 0.029 M  $\text{AgNO}_3$  and 0.1 M  $\text{NH}_3$  (see Equation 3.1). The membrane was then rinsed with water, and the second piece of tape was removed with ethyl acetate. Next, the gold plating bath for electroless deposition was prepared by combining 1.2 mL of the commercial gold plating solution, 0.2 g sodium sulfite, 2.4 mL of 37% formaldehyde solution, and 0.12 g  $\text{NaHCO}_3$  in 96 mL of water. Before treating the membrane, the pH of the plating bath was adjusted to  $\text{pH} \approx 7-8$  by the dropwise addition of 1 M sulfuric acid. The temperature of the bath was maintained at 4 °C. After about every 20 h of plating, the bath was replaced with a new plating solution. This replacement was done for 3 days. Then, this electroless deposition process was repeated with the concentration of the activation solution increased by 10-fold, and the concentration of the catalytic and plating solutions increased by 5-fold. This process was additionally performed with commercial AAO membranes from Whatman.

### **3.2.3. Electroless Deposition of Carbon Char into AAO**

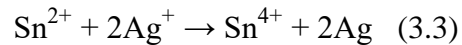
The carbon deposition process for the AAO templates was conducted using a slightly altered literature procedure by Boyer and Clarkson [18]. Carbonaceous material is combined with an activating agent, deposited onto the template, and then treated using a high temperature above 500 °C.

First, 20% w/w sucrose solution was prepared. Next, a ZnCl<sub>2</sub> solution was prepared with THF. These two solutions were combined in a 1:1 ratio with the ZnCl<sub>2</sub> to serve as the activating agent. Next, the combined solution was deposited dropwise onto four pieces of AAO, each with varying amounts of solution. The surface of the AAO pieces was cleaned after each deposition and then weighed to account for the increase in combined solution. After being weighed, the samples were dried by sitting it directly on a hot plate for approximately 1 min. Next, all of the samples were high temperature treated in a furnace chamber installed in the NCSU Forestry department. Under a constant flow of nitrogen gas flow at the rate of 1 L/min, the samples were heated according to a controlled temperature scheme at 5 °C/min to 620 °C. The temperature was held at 620 °C for 12 h before being cooled to room temperature.

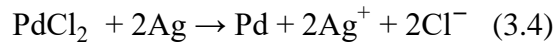
### 3.2.4. Electroless Deposition of Indium Tin Oxide into AAO

The indium tin oxide (ITO) deposition process for the AAO templates was conducted using a slightly modified literature procedure by Boehme et al [19]. The following reactions describe the chemistry behind the deposition process as reproduced from [19]:

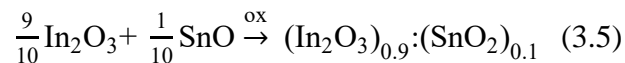
Activation:



Palladium Cluster Formation:



ITO Growth Mechanism:



First, commercial AAO membranes were annealed at 1250 °C/hour under vacuum ( $\sim 10^{-4}$  Torr), ramping at 10°C/min with a cooldown of 1°C/min. This annealing was done to reverse the surface electrostatic potential of the AAO from positive to negative to make it similar to the negative surface of polycarbonate membranes [20]. Once the samples were annealed, the AAO membranes were sensitized with 0.25 M SnCl<sub>2</sub> for 30 min at 45 °C. After incubation, the AAO was rinsed thoroughly and then incubated in an activation solution with 0.2 M AgNO<sub>3</sub> and 0.02 M Co(NO<sub>3</sub>)<sub>2</sub> for 15 min at room temperature. After thoroughly rinsing the AAO, the activation was completed by treating the sample with 0.2 M Pd(NO<sub>3</sub>)<sub>2</sub>, 0.015 M Ag<sub>2</sub>SO<sub>4</sub>, and 0.2 M HBF<sub>4</sub> for 20 min at room temperature and then rinsed. The final step of the process was the electroless deposition of the indium tin oxide (ITO). The activated membranes were treated with 0.27 M In(SO<sub>4</sub>)<sub>3</sub>, 0.03 M SnSO<sub>4</sub>, and 0.05 M (CH<sub>3</sub>)<sub>2</sub>NH•BH<sub>3</sub> for 15 min at room temperature. Before treating the membrane, the pH of the ITO solution was adjusted to pH $\approx$ 3-7 with the addition of 1 M NaOH. The ITO solution was heated for an hour to allow for all of the materials in the solution to dissolve.

### **3.2.5. Characterization of AAO Nanopores after Electroless Deposition**

Each deposited AAO sample was tested for initial conductivity with a voltmeter. In addition, the microstructure and morphology of all the deposited AAO samples were examined by the FEI Verios 460L SEM instrument installed and operated by the NCSU Analytical Instrumentation Facility (AIF). For SEM imaging, small pieces of AAO were broken from the larger membranes and mounted on a sample holder using double-sided carbon tape (Electron Microscopy Sciences). To suppress sample charging, low accelerating potentials (e.g., 500 V for FEI Verios 460L) were employed.

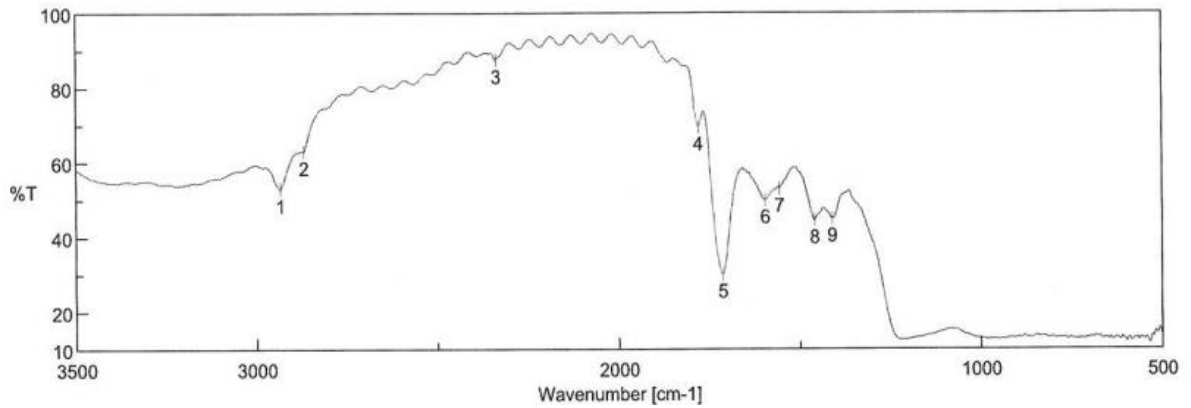
### 3.3. Results and Discussion

#### 3.3.1. Gold Deposition

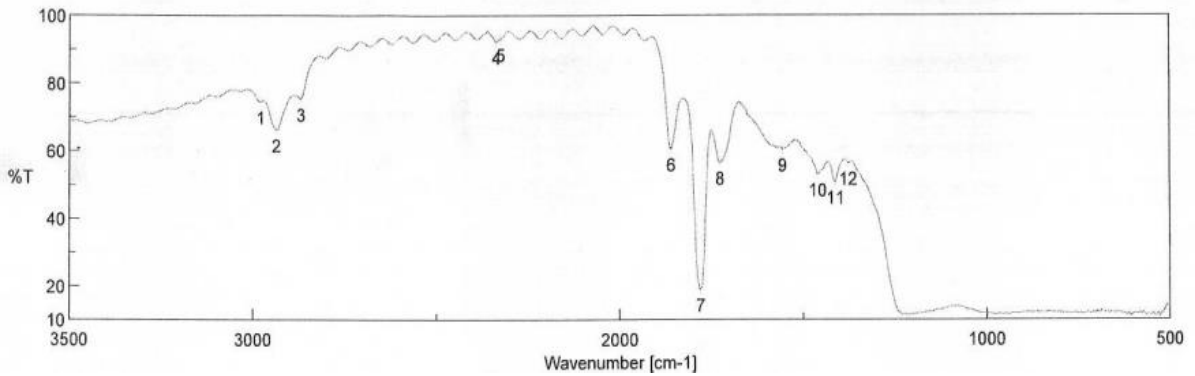
The essential steps in the surface modification procedures were the addition of SAPT to promote the activation of the membrane through  $\text{Sn}^{2+}$  chelation, masking the membrane surface to constrain the deposition of Au to only the nanopores, and decreasing pH of the plating solution to hinder the dissolution of the AAO membrane. The silanization of the AAO membrane from the SAPT solution was confirmed by measuring the absorption using FTIR. The IR spectrum obtained of the sample displayed a strong carbonyl stretch vibration band at  $1780.94\text{ cm}^{-1}$ , which indicated the attachment of the succinic anhydride groups to AAO (Figure 3.01). Next, the succinic anhydride groups were hydrolyzed to produce succinic acid residues, which allowed for the chelation of the  $\text{Sn}^{2+}$  onto the AAO. Upon hydrolysis, the anhydride absorption band disappeared while another strong band emerged at  $1711.51\text{ cm}^{-1}$ , corresponding to the absorption of the carboxylic carbonyls (Figure 3.02). Both IR spectra confirmed the silanization and hydrolysis of the AAO.

The masking approach of the AAO was supposed to inhibit the deposition of the Au on the surface and permit it only within the nanopores. In this case, the masking of the AAO failed to impede Au deposition on the surface. Ultimately, this masking issue contributed significantly to the poor pore deposition of the materials. While the membrane remained intact from a relatively neutral pH, Au was deposited onto the surface and a small amount into the AAO nanopores, shown by a yellowish-brown color change (Figure 3.03) and from the characterization using FE-SEM. The color change did not occur from contamination in the

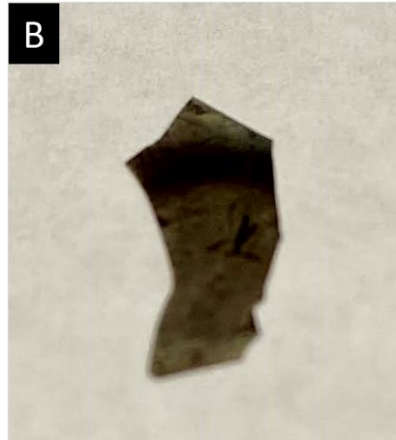
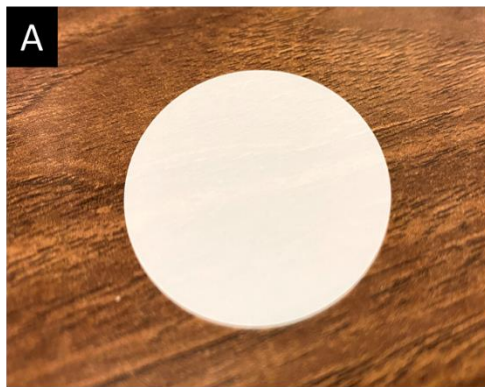
deposition process. There appeared to be no distinct change in the optical property compared to a typical smooth Au membrane surface [21].



**Figure 3.01** IR spectra of silanized AAO membrane after hydrolysis. Peak 5 shows the silanized AAO membrane was hydrolyzed at  $1711.51\text{ cm}^{-1}$ .

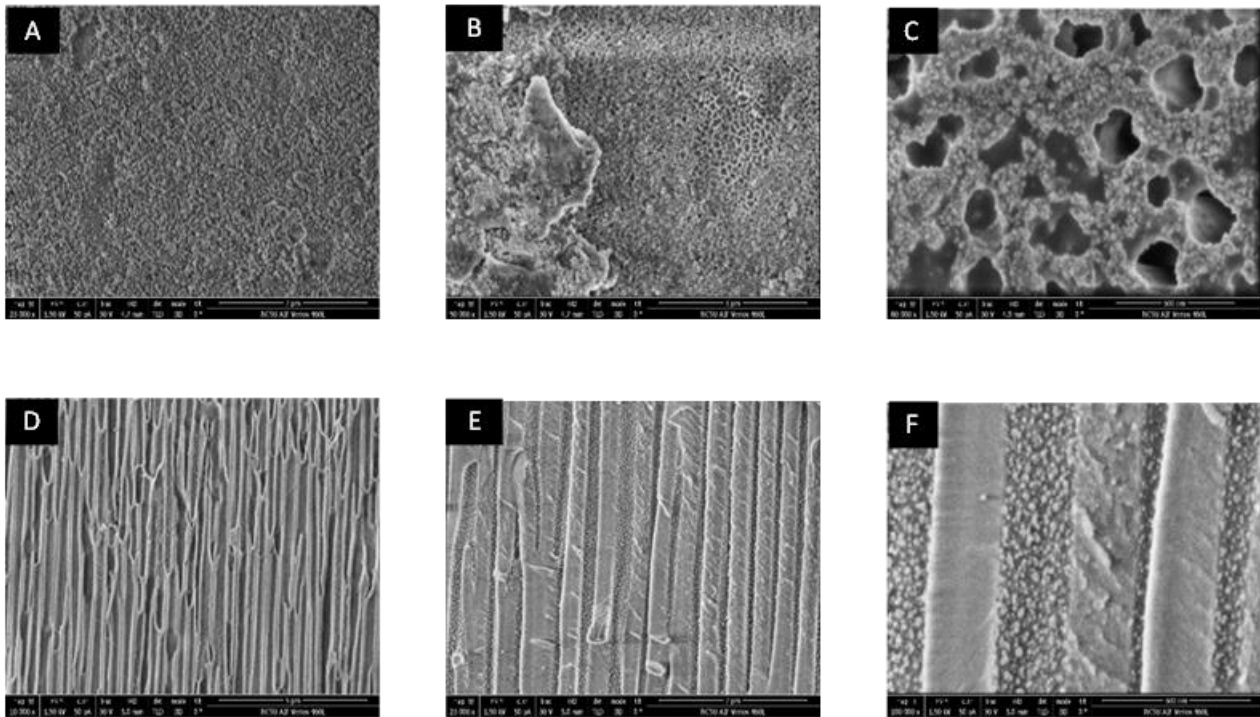


**Figure 3.02** IR spectra of silanized AAO membrane. Peak 7 shows the AAO membrane was silanized at  $1780.94\text{ cm}^{-1}$  after treatment in SAPT solution.



**Figure 3.03** Deposition of Au-AAO indicated by a color change from (A) white to (B) yellowish-brown.

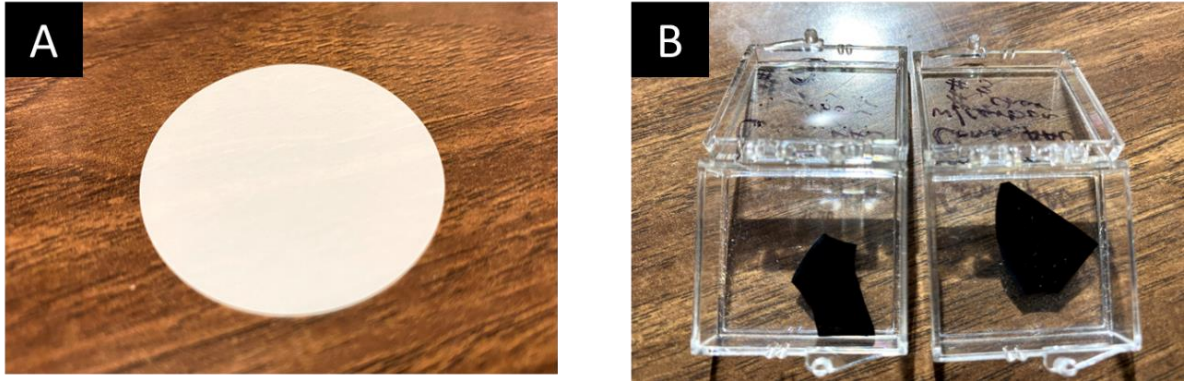
Figure 3.04 shows FE-SEM images of prepared Au-AAO. There are large Au clusters on the surface (Figure 3.04A-C) and smaller Au beads within the pores (Figure 3.04D-F). This aggregation suggests that the clusters are from a colloidal gold formation [22-24]. Because the Au-AAO was prepared by reducing a dissolved metal salt with a reducing agent, the Au from the plating solution was susceptible to aggregation of the atoms. This clustering typically serves to control the growth of Au nanotubes. For this experiment, the aggregation obstructed the full diffusion of the Au into the AAO nanopores since the larger clusters are bigger than the AAO pore size, as shown in Figure 3.04B.



**Figure 3.04** FE-SEM images of Au-AAO deposition on the surface and within the pores. (A-C) Clusters of Au material sit on the surface of the AAO membrane. (D-F) Cross-sectional images show smaller beads of Au material that lie along the walls of the AAO nanopores.

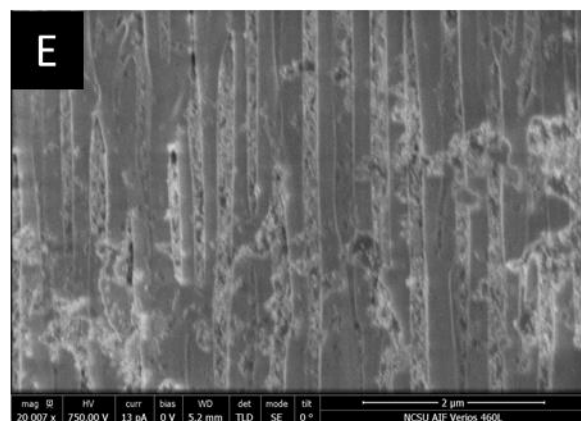
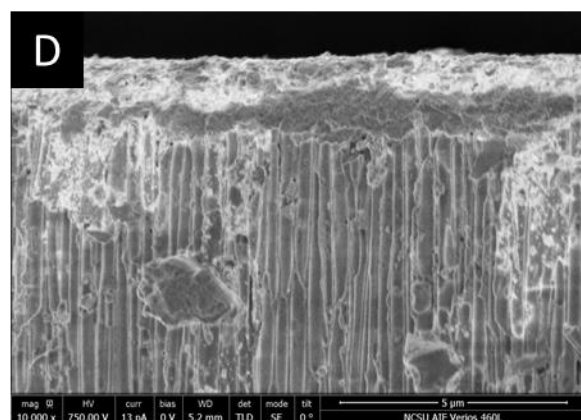
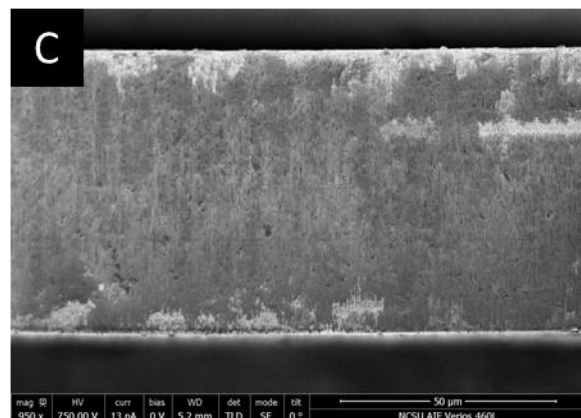
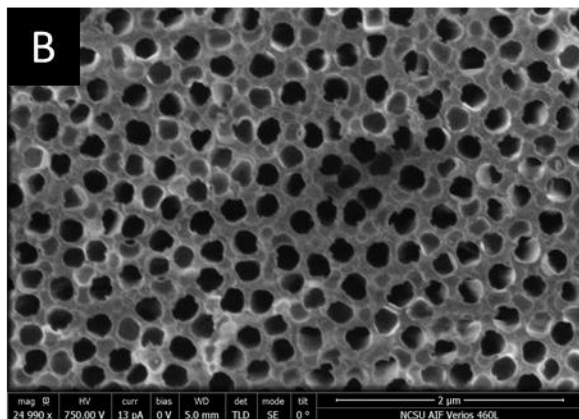
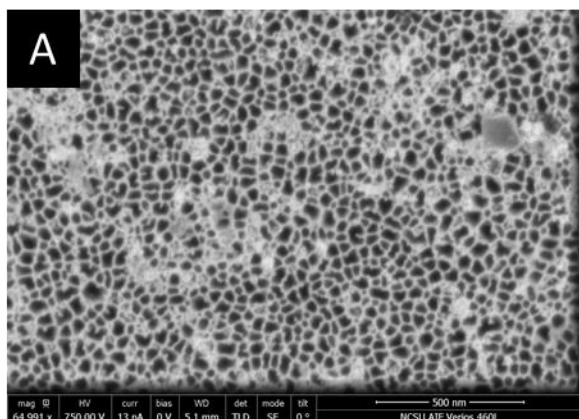
### 3.3.2. Carbon Char Deposition

Sucrose was combined with the activating agent,  $ZnCl_2$ , and then treated at a high temperature of 620 °C after deposition onto the AAO membrane to allow for carbonization to occur. This carbonization was confirmed through a color change from white to black, as shown in Figure 3.05.



**Figure 3.05** Deposition of carbonaceous material into AAO nanopores and development of carbon char indicated by a color change from (A) white to (B) black.

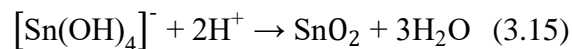
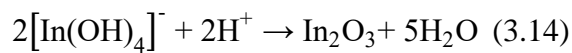
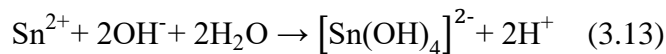
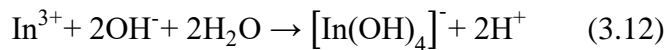
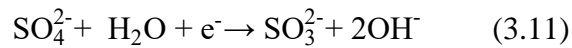
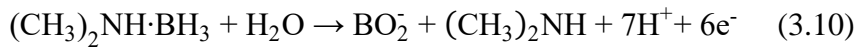
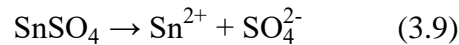
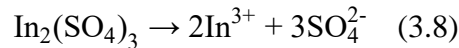
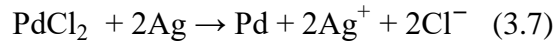
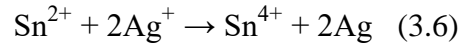
Furthermore, FE-SEM images provide additional confirmation of the deposition of carbonaceous material into the AAO pores and on the surface, as shown in Figure 3.06.

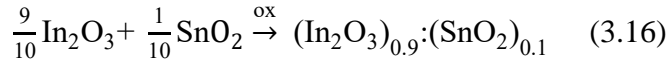


**Figure 3.06** FE-SEM images of carbon char AAO. (A-B) Surface of the AAO membrane with carbon char. (C-E) Cross-section of AAO with carbonaceous material deposited deeper into the nanopores.

### 3.3.3. Indium Tin Oxide Deposition

To begin the process of the Indium Tin Oxide (ITO) deposition, the mechanisms of the process associated with the procedure were reviewed. It was noted that the initial step dealt with an activation of the AAO membrane through the reduction of  $\text{Ag}^+$  and the oxidation of  $\text{Sn}^{2+}$ . Next, another redox reaction was carried out on the AAO by oxidizing  $\text{Ag}^0$  to  $\text{Ag}^+$  and reducing  $\text{Pd}^{2+}$  to  $\text{Pd}^0$ , leading to the formation of palladium clusters on the surface and within the pores. The final step involved the increase of  $\text{OH}^-$  concentration, which resulted from the combination of the  $\text{OH}^-$  with  $\text{In}^{3+}$  and  $\text{Sn}^{2+}$  to generate  $\text{In}(\text{OH})_3$  and  $\text{Sn}(\text{OH})_2$ ; followed by the production of ITO from a 9:1 concentration ratio of  $\text{In}_2\text{O}_3$  and  $\text{SnO}_2$  that replaces the previous palladium clusters. By carefully adjusting pH of the solution used for ITO deposition, the growth of nanotubes could be controlled. A summary list of the equations of the main steps involved in the deposition process based on Boehme et al. is reproduced here for reference:



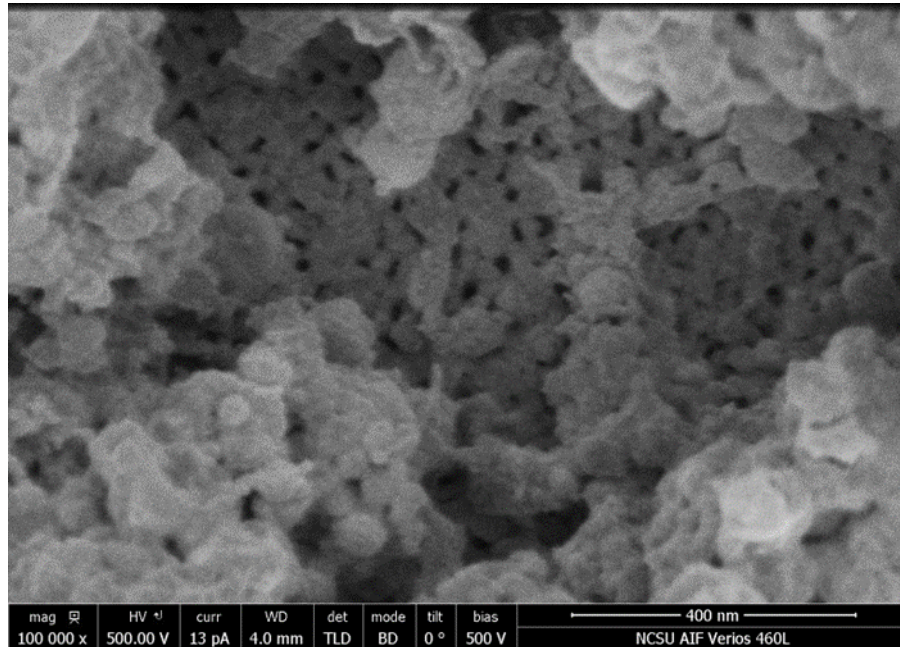


After several attempts of the full deposition process, it was determined that the procedure as described in the referenced paper was irreproducible.

Multiple inconsistencies within the process, as well as the failure to reproduce the reference results, led to the conclusion that the possibility of reproducing the results is rather slim. For the activation step, both  $\text{AgNO}_3$  and  $\text{Co}(\text{NO}_3)_2$  were used in the solution. It has been previously established from the gold deposition that  $\text{Ag}^+$  aids in activating the AAO membrane by oxidizing the  $\text{Sn}^{2+}$  and reducing it to  $\text{Ag}^0$ . It is unclear as to why  $\text{Co}(\text{NO}_3)_2$  was used in this step. However, it is suspected that it might have served as a catalyst. In the literature text, the significance of the Co material was never discussed in further detail. In addition, before treating the membrane, the pH of the ITO solution was adjusted to  $\text{pH} \approx 3-7$  by the addition of 1 M NaOH. Because  $\text{In}_2(\text{SO}_4)_3$  is highly acidic and becomes insoluble above  $\text{pH} \approx 3$ , the solution was insoluble for the given pH range ( $\text{pH} \approx 3-7$ ) compared to the article. Even after heating the ITO solution to dissolve all of the materials, a precipitate remained instead of forming a solution.

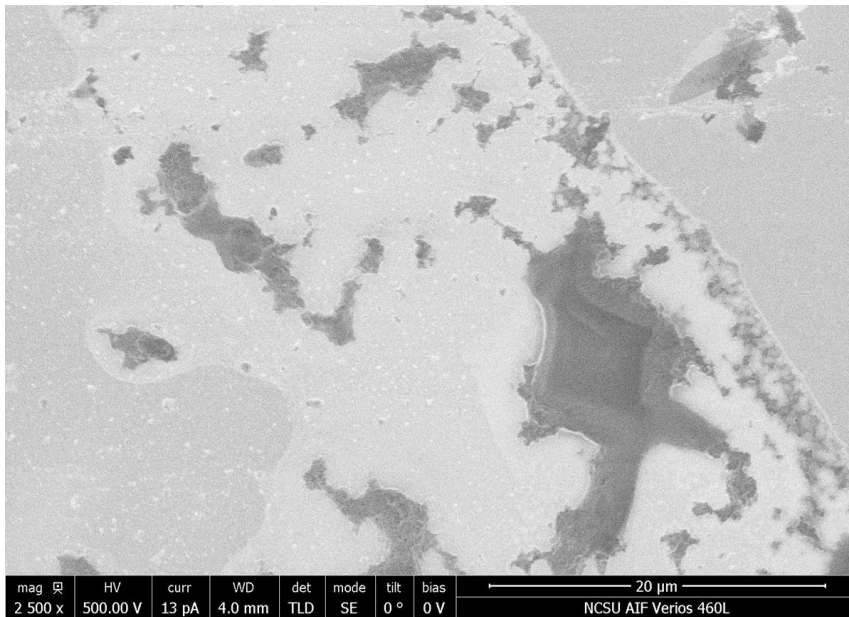
Another problem that may have affected the deposition was the surface electrostatic potential of the AAO membrane. This appears to be positive as opposed to the negative surface potential of the polycarbonate membrane, which was used in the original article. To test this, the surface electrostatic potential of the AAO was determined by annealing at temperatures above 1100 °C [20,25]. It was observed that, even with this change, there was no ITO nanotube growth.

Figure 3.07 shows none of the ITO deposited into the pores of the AAO, but there was material aggregated on the surface.



**Figure 3.07** AAO membrane with aggregation of ITO material on the surface. This major accumulation on the surface inhibits deposition of ITO into the pores.

To gather the material accumulated on the AAO surface and confirm that no ITO nanotubes were produced, we dissolved the membrane in 1 M NaOH. Only clusters of material were shown in the FE-SEM images, as presented in Figure 3.08. This electroless deposition procedure was repeated with a polycarbonate membrane to replicate the original literature results. Using the polycarbonate membrane, it was impossible to yield ITO nanotubes (Figure 3.09) due to the large ITO clusters remaining on the surface of the membrane.



**Figure 3.08** ITO material after dissolving the AAO membrane.

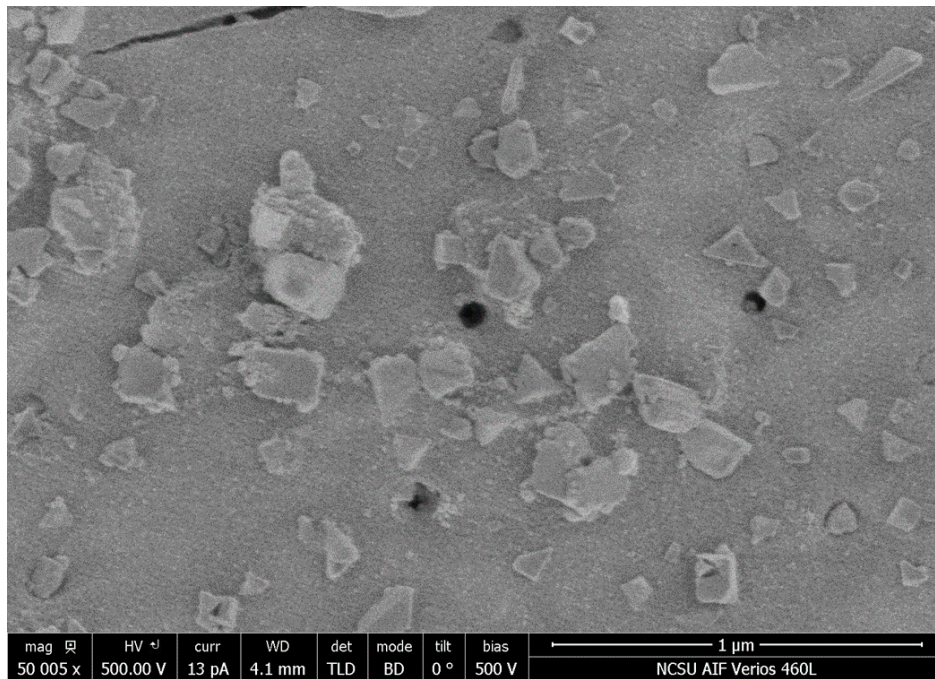


**Figure 3.09** Polycarbonate membrane with ITO deposition. Clusters of ITO material remained on the surface without deposition into the pores.

### 3.3.4. Conductivity Test

Electrical conductivity measurements were conducted by placing the probes of a voltmeter on the AAO and observing the resistivity of the membrane. A schematic of the conductivity test is provided in Figure 3.10. The resistance of a material is the reciprocal to the conductivity. Therefore, lower resistance will yield a higher conductivity. For each of the deposited samples, there was no resistance displayed. As shown in the schematic, the deposited material in the AAO pores is not likely to protrude above the pores on the AAO surface.

For this reason, the probes would be unable to make adequate electrical contact with the materials in the pores, especially with the probes being much larger than the pores at the nanoscale level. Since the AAO is an insulator, there will be no conductivity displayed. To attempt to make better contacts with the surface with the probes, liquid metal was applied to the surface to provide sufficient electrical contact. However, due to the hydrophobic nature of the surface, the metal would not remain on the surface. From the FE-SEM images, most of the electroless deposition occurred on the membranes' surface. To initially resolve the issue of nonconductivity, two pieces of sample-sized aluminum sheets were attached to the ends of both voltmeter probes, and the deposited AAO samples were sandwiched between the sheets in an attempt to ensure complete contact. With little to no deposition in the pores, it was impossible to have conductivity through the material since there was limited contact through the pores, and no conductivity could be detected.

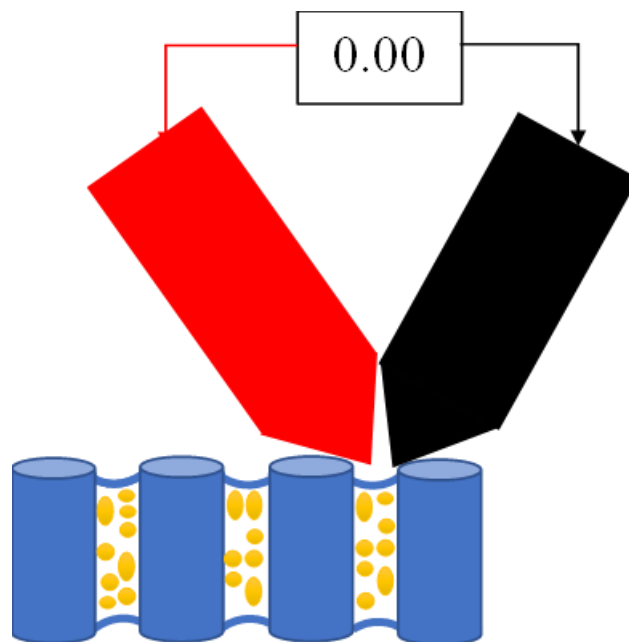


**Figure 3.10** Schematic of conductivity test of electroless deposited AAO samples.

Subsequently, it was deduced that an insufficient amount of ITO material was exposed from the pores above the AAO surface. Therefore, for any conductivity measurement to occur, the materials must be deposited completely in the pores of the AAO and emerge from both sides of the membrane pores in order to guarantee detectable conductivity.

### **3.4. Conclusion**

Electroless deposition strategies to deposit conductive materials within the AAO membrane nanopores were explored using Au, carbon char, and indium tin oxide (ITO). The strategies for Au and carbon char resulted in deposition. However, there was limited diffusion of the materials into the nanopores; most of the material clustered on the surface of the AAO membrane. For ITO deposition, the strategy based on a previous literature procedure had several discrepancies in the deposition process and could not be reproduced. Therefore, no

deposition of ITO occurred. With little to no deposition of any of the materials in the pores, it was impossible to have conductivity through the AAO membrane since there was limited contact of the materials through the pores. Consequently, no conductivity could be detected.

Although the electroless deposition did not yield desired results, this technique of chemically depositing conductive materials is still of interest as a potential application for template-based study. For example, the deposition of ITO into the AAO nanopores could be simplified and improved upon by using 2-methoxyethanol as the solvent [26]. The ITO is prepared in solution and allowed to deposit into the AAO nanopores evenly. In contrast to the various chemicals and reactions in the deposition process from the literature reference, this method uses fewer chemicals to achieve ample ITO deposition. Furthermore, this process enables greater deposition of ITO through the AAO nanopores. Thus, this leads to better conductivity through the AAO membrane. With the acquired conductive property, these advanced membranes could be utilized to gain more insight into the interactions between the nanoporous membranes and biomolecules and the surface electrostatic properties of these nanopore-confined biomolecules.

### 3.5. References

1. Keller, F.; Hunter, M.S.; Robinson, D.L. *Structural Features of Oxide Coatings on Aluminum*. Journal of electrochemical society, 1953. **100**: 411.
2. Dell'Oca, C.J.; Pulfrey, D.L.; Young, L. *Anodic Oxide Films. In Physics of Thin Films*; Elsevier: Amsterdam, The Netherlands, 1971; Volume 6, pp. 1–79.
3. Diggle, J.W.; Downie, T.C.; Goulding, C.W. *Anodic oxide films on aluminum*. Chemical reviews, 1969. **69**: 365–405.
4. Henley, V.F. *Anodic Oxidation of Aluminium and Its Alloys: The Pergamon Materials Engineering Practice Series*; Elsevier Science: Kent, UK, 2014
5. Lee, W.; Park, S., *Porous Anodic Aluminum Oxide: Anodization and Templated Synthesis of Functional Nanostructures*. Chemical reviews, 2014, **114**: 7487-7556.
6. Martin, C.R. *Nanomaterials: A Membrane-Based Synthetic Approach*. Science, 1994. **266**: 1961.
7. Patella, B.; et al. *Anodic Alumina Membranes: From Electrochemical Growth to Use as Template for Fabrication of Nanostructured Electrodes*. Applied science, 2022. **12**: 869.
8. Nishizawa, M.; Menon, V.P.; Martin C.R. *Metal nanotubule membranes with electrochemically switchable ion-transport selectivity*. Science, 1995. **268**: 700.
9. Quinn, B.M.; Dekker, C.; Lemay, S.G. *Electrodeposition of Noble Metal Nanoparticles on Carbon Nanotubes*. Journal american chemical society, 2005. **127**: 6146.
10. Hiruma, K. et al. *Growth and optical properties of nanometer-scale GaAs and InAs whiskers*. Journal of applied physics, 1995. **77**: 447.
11. Martin, C.R. *Template synthesis of polymeric and metal microtubules*. Advanced materials, 1991. **3**: 457-459.
12. Martin, C.R.; Parthasarathy, R.V. *Polymeric Microcapsule Arrays*. Advanced materials, 1995. **7**: 487.
13. Parthasarathy, R.V.; Phani, K.L.N.; Martin, C.R. *Template Synthesis of Graphitic Nanotubules*. Advanced materials, 1995. **7**: 896.
14. Kruk, M. et al. *Synthesis of Mesoporous Carbons Using Ordered and Disordered Mesoporous Silica Templates and Polyacrylonitrile as Carbon Precursor*. Journal of physical chemistry B, 2005. **109**: 9216.

15. Boehme, M.; et al. *Room temperature synthesis of indium tin oxide nanotubes with high precision wall thickness by electroless deposition*. Beilstein journal of nanotechnology, 2011. **2**: 119-126.
16. Zhang, S-H.; et al. *Synthesis of silver nanotubes by electroless deposition in porous anodic*
17. *aluminium oxide templates*. Chemical communication, 2004.: 1106–1107.
18. Kohli, P., et al. *Template Synthesis of Gold Nanotubes in an Anodic Alumina Membrane*. Journal of nanoscience and nanotechnology, 2004. **4**(6): 605-610.
19. Boyer, S. J.; Clarkson, R. B. *Electron paramagnetic resonance studies of an active carbon: The influence of preparation procedure on the oxygen response of the linewidth*. Colloids and surfaces, 1994. **82**: 217-224.
20. Boehme, M.; et al. *Room temperature synthesis of indium tin oxide nanotubes with high precision wall thickness by electroless deposition*. Beilstein journal of nanotechnology, 2011. **2**: 119-126.
21. Kovaleva, E. G.; et al. *Electrostatic properties of inner nanopore surfaces of anodic aluminum oxide membranes upon high temperature annealing revealed by EPR of pH-sensitive spin probes and labels*. Journal of membrane science, 2020. **604**: 118084.
22. Altunas, S.; Buyukserin, F. *Fabrication and characterization of conductive anodic aluminum oxide substrates*. Applied surface science, 2014. **318**: 290-296.
23. Polte, J. *Fundamental Growth principles of colloidal metal nanoparticles – a new perspective*. CrystEngComm, 2015. **17**: 6809-6830.
24. Toshima, N.; Yonezawa, T. *Bimetallic nanoparticles – novel materials for chemical and physical applications*. New journal of chemistry, 1998. 1179-1201.
25. Turkevich, J.; Stevenson, P.C.; Hillier, J. *The Formation of Colloidal Gold*. Journal of physical chemistry, 1953. **57**: 670-673.
26. Keesom, W.H., Zelenka, R.L., Radke, C.J. *A Zeta-Potential Model for Ionic Surfactant Adsorption on an Ionogenic Hydrophobic Surface*. Journal of colloid and interface science, 1988. **125**: 575-585.
27. Zhang, H. J. *Synthesis of indium tin oxide nanotubes using 2-methoxyethanol as solvent via simple template method*. Journal of alloys and compounds, 2010. **504**: 171-176

## **CHAPTER 4: SURFACE ELECTROSTATIC POTENTIAL OF NANOPORE- CONFINED PHOSPHOLIPID BILAYER IN HIGH-TEMPERATURE ANNEALED AAO SUBSTRATE REVEALED BY SPIN-LABELING EPR OF A PH-SENSITIVE NITROXIDE**

### **4.1. Introduction**

Lipid bilayer membranes play a pivotal role in biology and also in energy transduction events occurring during photosynthesis. While some of these roles are undoubtedly structural in nature, others may be related to the electronic structure, as indicated by the need for lipids with an anionic headgroup, such as PG lipids. These lipids cause the surface of cellular membranes to be negatively charged, affecting many of the cellular processes. For this project, we decided to focus on POPG (1-palmitoyl-2-oleoyl-sn-glycero-3-phospho-(1'-rac-glycerol), which is a negatively charged lipid.

Surface electrostatic potential is one of the essential properties of the bilayer membrane as it determines interactions of other molecules with the bilayer. For example, the surface potential affects the concentration of ions and other small molecules in the immediate vicinity of the bilayer [1] and facilitates intercellular and intracellular recognition and transport [2-3]. Because of a significant gradient of ion concentration at the bilayer interface, it is imperative to measure lipid bilayer electrostatic potential at well-defined positions with respect to the bilayer-water interface in order to further decipher the mechanisms of electrostatically driven biological phenomena in cells.

Currently, the group of analytical methods suitable for assessing the surface electrostatic potential of lipid bilayers is limited in its technical capabilities and comparisons. It mainly consists of atomic force microscopy [4-5], interaction force measurements [6], fluorescent spectroscopy [7-9], NMR [10-12], and spin-label EPR (13-20). Unfortunately, most of these methods suffer substantially when larger bilayer membrane systems are involved. Typically, spin-label EPR studies of bilayer electrostatics provide a wealth of data on the structure of these lipid systems. This technique aids in evaluating bilayer electrostatics by observing reversible ionization of EPR molecular probes upon pH titration. However, one of the limitations of this method is the ambiguity of the exact location of the measured potential because the locations of the partitioned EPR probe molecules in regard to the bilayer surface are largely unknown.

Previously, SSLBs were developed to investigate the arrangement and functionality of lipid membranes by magnetic resonance, as explained in Chapter 1. However, the above-mentioned lipid membrane mimetics could only be formed from a relatively narrow class of lipids and lipid-like molecules and have several other restrictions such as temperature, pH, ionic strength, etc. More recently, anodic aluminum oxide (AAO) membranes with macroscopically ordered, homogeneous nanopores of tunable diameter were utilized to promote the self-assembly of lipid nanotubular bilayers inside the pores. The macroscopic alignment of the lipid assemblies provided by such structures assists in characterizing the biophysical properties of nanopore-confined molecules by magnetic resonance methods, such as NMR and spin-label EPR.

In this work, we used a spin-label EPR titration method described in [21] to access surface electrostatic potential of AAO substrate-supported lipid multilamellar vesicles (MLVs). A pH-sensitive phospholipid-based nitroxide probe (IMTSL-PTE) synthesized at NCSU was fully integrated into the lipid bilayer with minimal perturbation. The spin-labeled lipids were deposited onto the nanoporous substrate, allowed to self-assemble into cylindrical phospholipid nanotubes in the pores, subjected to various pH buffers, and then characterized by EPR. Once positioned at the membrane surface with surrounding charged and uncharged species, the EPR spectra of the membrane probe report directly on the protonated and non-protonated forms of the nitroxide moiety since they have different magnetic parameters. This spectroscopic data of IMSTL-PTE results in the observed  $pK_a$  of the probe as a function of the bilayer electrostatic surface potential, which ultimately aids in its determination.

The observed  $pK_a$  (or interfacial  $pK_a^i$ ) of the spin probe at the membrane-water interface of the bilayer surface differs from the  $pK_a$  of the probe in pure bulk water, intrinsic  $pK_a^0$  (Equation 4.1). This difference is attributed to two Gibbs free energy components,  $\Delta G_{pol}$  that is required to relocate the charged probe from bulk aqueous solution to an interface with different local electrical permittivity,  $\epsilon_i$ , and  $\Delta G_{el}$  that is ascribed to the local electrostatic potential,  $\Psi$ . As a result, the overall equilibrium between charged and uncharged species around the surface is altered. Because  $pK_a = -\log_{10}(K_a)$ , where  $K_a$  is the equilibrium constant of protonation of the nitroxide moiety tertiary amino group, the interfacial  $pK_a^i$  of the probe is expressed as:

$$pK_a^i = pK_a^0 + \Delta pK_a^{el} + \Delta pK_a^{pol} \quad (4.1)$$

where  $\Delta pK_a^{pol}$  and  $\Delta pK_a^{el}$  are contributions from the polarity shift and the surface electrostatic potential, respectively [7,9,15].

In relation to  $\Delta pK_a^{el}$ , the surface electrostatic potential can be determined as:

$$\Delta pK_a^{el} = \frac{-e\Psi}{\ln(10)kT} \quad (4.2)$$

where  $e$  is the elementary charge,  $k$  is the Boltzmann constant, and  $T$  is the absolute temperature.

In order to determine  $\Delta pK_a^{el}$ , the other contributions to  $pK_a^i$ ,  $pK_a^0$  and  $\Delta pK_a^{pol}$ , must be measured at the desired temperature of the full experiment since the interfacial  $pK_a^i$  is temperature dependent. The intrinsic  $pK_a^0$  can be obtained by experimentally titrating a model spin probe. M. Voinov et al. synthesized water-soluble IMTSL-2-mercaptoethanol (IMTSL-ME) adduct to model IMTSL-PTE and found the intrinsic  $pK_a^0$  to be  $3.33 \pm 0.03$  from EPR titrations [1]. In contrast,  $\Delta pK_a^{pol}$  could be influenced by the location of the probe with respect to the bilayer surface, along with chemical moieties in the surrounding area. M. Voinov et al. resolved by measuring  $pK_a^i$  for a probe incorporated into a model bilayer system with a chemically similar but uncharged interface, the electrostatic shift is absent, and also  $\Psi=0$  and  $\Delta pK_a^{el}=0$  [1]. Therefore, the observed  $pK_a$  difference should be entirely attributed to  $\Delta pK_a^{pol}$ . The surfactant Triton X-100 was selected as the reference system since it lacks any charged species. Triton X-100 forms micelles that can be employed as a nonpolar electrically neutral model interface between the aqueous phase and lipid-like phase. The IMTSL-PTE probes were integrated into Triton X-100 micelles and allowed the authors to calculate for the polarity shift

$\Delta pK_a^{pol}=0.81\pm 0.03$  with the previous intrinsic  $pK_a^0$  at 17 °C. Using the previously determined intrinsic  $pK_a^0$  and experimentally determined  $\Delta pK_a^{pol}$ , the  $\Delta pK_a^{el}$  of the AAO SSLBs can be determined from Equation 4.2.

As referred to in Chapter 2, the AAO substrates can experience defects in the oxide layer that stem from minor impurities in the surface state of the starting metal before anodization or to the anions incorporated from the electrolyte solution after anodization [55]. Because of these defects, a background signal of the AAO substrate is observed in the EPR spectra amongst the signal of the spin probe. Additionally, for AAO with smaller pore diameter (<50 nm), the apparent pH of the inner channels will be lower than the bulk pH [22], which will significantly impact the spectra of the lipid samples. In order to diminish AAO background signal from defects and improve the overall spectra, the AAO substrate must be annealed at high temperatures above 500 °C. In this chapter, we report on the effect of high-temperature annealing of the AAO substrate on the measurement of surface electrostatics of POPG lipid bilayers revealed with spin-labeling EPR of IMTSL-PTE.

## **4.2. Experimental Section**

### **4.2.1. Materials and Chemicals**

1-palmitoyl-2-oleoyl-sn-glycero-3-phospho-(1'-rac-glycerol) (POPG) lipids (>99% pure) was purchased from Avanti Polar Lipids (Alabaster, AL) as a chloroform solution and stored at -80 °C before use without any further purification. IMTSL-PTE was provided by Dr. Max Voinov and synthesized as described elsewhere [21]. All other chemicals were purchased from Sigma-Aldrich (St. Louis, MO), Acros Organics (Morris Planes, NJ), Sigma Aldrich/Merck,

KGaA (Darmstadt, Germany), or VWR International, LLC (Radnor, PA, USA) unless otherwise indicated.

#### **4.2.2. Preparation of AAO Substrates with Homogeneous Pore Distribution**

The AAO substrates were prepared in-house by a two-step anodization process similar to the one described by Masuda and Fukuda [23]. A high-purity aluminum foil (99.99%, 0.127 mm thick, Strem Chemicals, Inc., Newburyport, MA, USA) was utilized as the starting material. An aluminum foil was cut into 3 by 2 cm strips. Each strip was anodized in 4 wt% oxalic acid for 2 h at 40 V. Afterwards, the initial alumina oxide formed on the aluminum foil was subsequently stripped down in a mixture of 3.5%  $\text{H}_3\text{PO}_4$  and 45 g/L of  $\text{CrO}_3$  at 87 °C for about 10 min and then washed thoroughly in deionized water. Immediately following this procedure, the aluminum foil was re-anodized for 1 h. A thin layer of a household nail polish (Sally Hansen, Coty Inc., New York, NY), was then applied to one side of the foil in order to protect it from further anodization. Once thoroughly dried, the anodization step continued at 40 V for about 32-40 h, depending on the desired pore length of ~35-45 nm. After completing the anodization, the nail polish was removed with acetone. Next, the thin back-side oxide layer was removed by floating the aluminum piece on the surface of 10%  $\text{H}_3\text{PO}_4$  for about 2 hrs at room temperature. The remaining metallic aluminum was dissolved in 10%  $\text{CuCl}_2$  solution at room temperature under mild sonication, leaving the alumina oxide. To completely open up the nanopores from the barrier side, as well as to enlarge the pores to a desired diameter, the alumina oxide piece was subsequently treated with 5%  $\text{H}_3\text{PO}_4$  aqueous solution for a controlled amount of time (typically 0.5-1 h for pore diameter ~35-45 nm).

The pore morphology and structure of all the fabricated AAO were examined by FEI Verios 460L SEM instrument installed and operated by the NCSU Analytical Instrumentation Facility (AIF). For SEM imaging, small pieces of AAO were broken from the larger membranes and mounted on a sample holder using double-sided carbon tape (Electron Microscopy Sciences). Low accelerating potentials (e.g., 500 V) were employed to suppress sample charging. The pore diameters were analyzed directly from the SEM images using ImageJ (NIH) software.

#### **4.2.3. High-Temperature Annealed Nanoporous AAO Substrates**

For annealing at 800 °C, the AAO substrates were heated on a ceramic plate to 800 °C at 1°C/min ramp for 3 h in a 62700 Furnace (Barnstead Thermolyne Corporation, Ramsey, MN).

#### **4.2.4. Preparation of Spin-labeled Lipid Vesicles**

Spin-labeled multilamellar vesicles (MLVs) were prepared by mixing chloroform solutions of POPG lipids with 1 mol % of IMTSL-PTE or MTSL-PTE. Organic solvents were evaporated with a nitrogen stream yielding a thin lipid film on the surface of a 5-mL conical glass vial. Residual solvent was removed by evacuating the vial in a vacuum desiccator connected to a rotary pump overnight. The dried lipid films were rehydrated by adding 400-500 µL of 50 mM phosphate buffer at pH=7.00 and then subjected to about 10 consecutive freeze-thaw cycles between liquid nitrogen and a water bath at 37 °C to disrupt large aggregate of lipids. The final lipid concentration was ~20 w/w %.

#### **4.2.5. Preparation of Spin-labeled Lipid Vesicles Doped with Gramicidin A**

Spin-labeled MLVs were prepared by mixing chloroform solutions of the POPG lipids with 1 mol % of IMTSL-PTE or MTSL-PTE and 1:300 mol of gramicidin A to POPG lipids. MLVs were prepared as above. The final lipid concentration was ~20 w/w %.

#### **4.2.6. Preparation of AAO Nanopore-confined POPG MLVs**

Approximately 10  $\mu$ L aliquot of lipid suspension was pipetted onto the surface of laser-cut AAO strips (3x8 mm<sup>2</sup>). The lipids were allowed to enter the nanopores (~35-45 nm pore diameter, 57  $\mu$ m pore length) and dry at ambient conditions on a Teflon plate overnight. Then, the strips were rehydrated for measurement by dripping aqueous buffer with the desired pH onto the AAO piece.

#### **4.2.7. pH adjustment of 50mM Phosphate Buffers**

Approximately 0.5 mL of phosphate buffer was placed into a 1.5-mL Eppendorf tube and pH of the bulk solution was adjusted by titration with a 0.1 M HCl solution or a 0.05 M NaOH solution. The pH was measured by an Orion pH electrode 98 series (Thermo Scientific, Beverly, MA) at 17 °C to remain consistent with the temperature of the overall EPR experiment.

#### **4.2.8. pH adjustment of AAO Nanopore-confined Lipid Bilayers**

AAO strips with deposited lipid suspension were inserted into a flat EPR capillary and then placed into a buffer solution (2 ml) with required pH for 30 min at 17 °C. To ensure complete

pH equilibrium, the SSLBs were measured after each buffer exchange for 30 min until there was no change in EPR spectra.

#### **4.2.9. EPR measurements**

All nanopore-confined lipid samples were measured using continuous-wave (CW) EPR spectroscopy at X-band (9.5 GHz) to follow pH-induced changes in magnetic parameters of the spin-labeled phospholipid. The buffer solutions were drawn into a miniature hollow glass tube (i.d. = 0.1 mm, VitroTubes™, Mountain Lakes, NJ), the ends of the capillary were sealed with Critoseal® (Leica Microsystems Inc., Buffalo Grove, IL). Enclosing the samples in the rectangular glass tubing prevented water evaporation from the nanopores. The samples were examined visually before and after the EPR measurement to ensure that the nanopores remained filled with the buffer solutions.

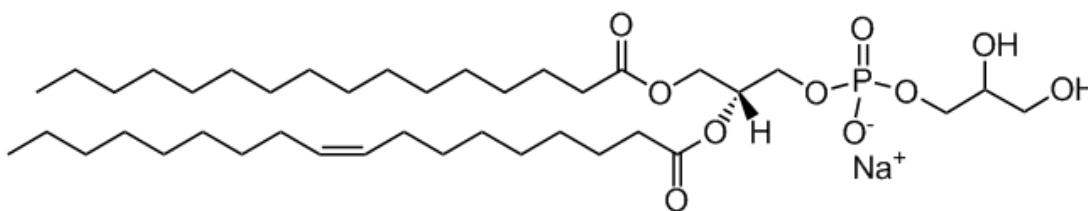
EPR spectra were recorded at 17 °C with a Varian E-109 (Varian Inc., Palo Alto, CA) spectrometer interfaced to a PC and digitized to 2048 data points. When using the Varian spectrometer, the sample temperature was maintained by a digital variable temperature accessory with a stability better than +/-0.02 °C and a gradient below 0.07 °C/cm over the sample region [24].

### **4.3. Results and Discussion**

#### **4.3.1. Choice of Lipids for Model Bilayer Systems**

Phosphatidylglycerol (PG) lipids are the most abundant anionic lipids in nature and make up most of the cellular membrane for prokaryotic cells, such as bacteria or plants. Because of their

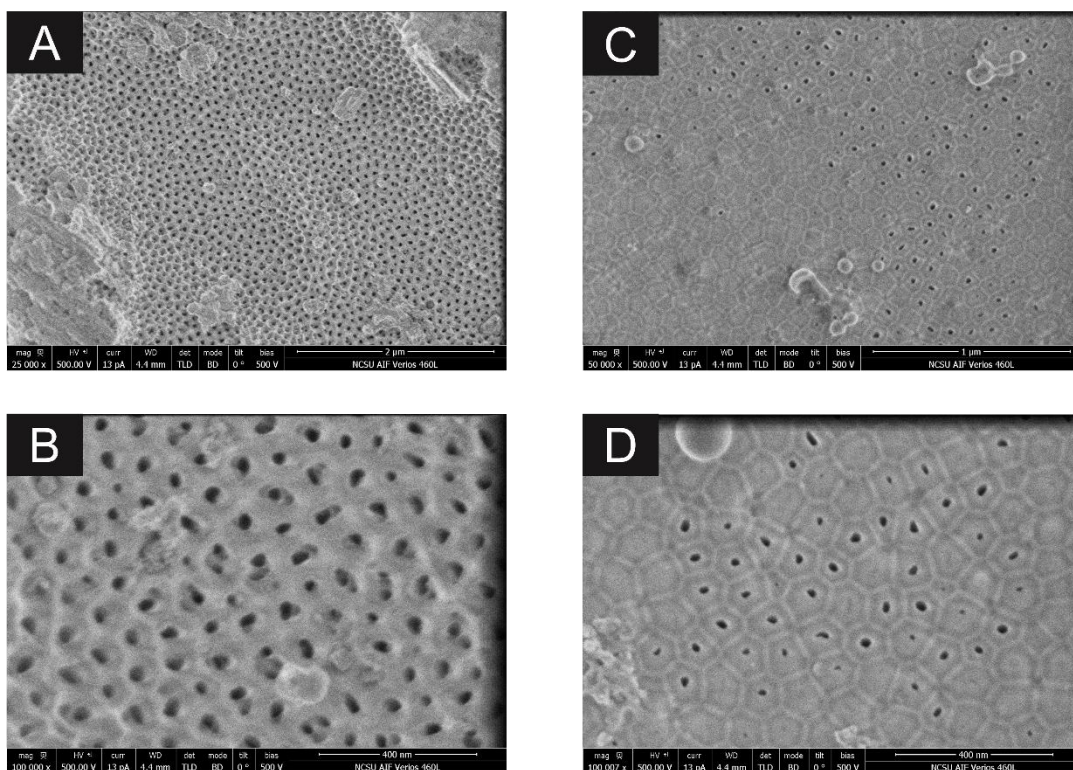
negative charge, they cause the surface of cellular membranes to also be negatively charged. Additionally, anionic lipids such as PG lipids play many roles in cellular function due to their basic and electronic structure. As a result, PG lipids have been extensively used as constituents of model membranes in studies [25-30]. Lipid bilayers formed from the longer-chain, unsaturated POPG lipid undergo a main phase transition temperature of  $T_m = -2\text{ }^\circ\text{C}$ . For a fixed headgroup structure, the hydrophobic tails of the lipids can take many different forms and govern the phase of the lipid bilayer. By reducing the chain length or increasing the number of unsaturated bonds in the chains, a lower  $T_m$  can be achieved. Thus, the low  $T_m$  makes POPG lipids a rather convenient model for biophysical studies of membrane properties because it guarantees the biologically relevant fluid phase for these lipid systems when subjected to a wide range of pH and ionic strength conditions at or slightly below room temperature.



**Figure 4.01** Chemical structure of POPG lipid.

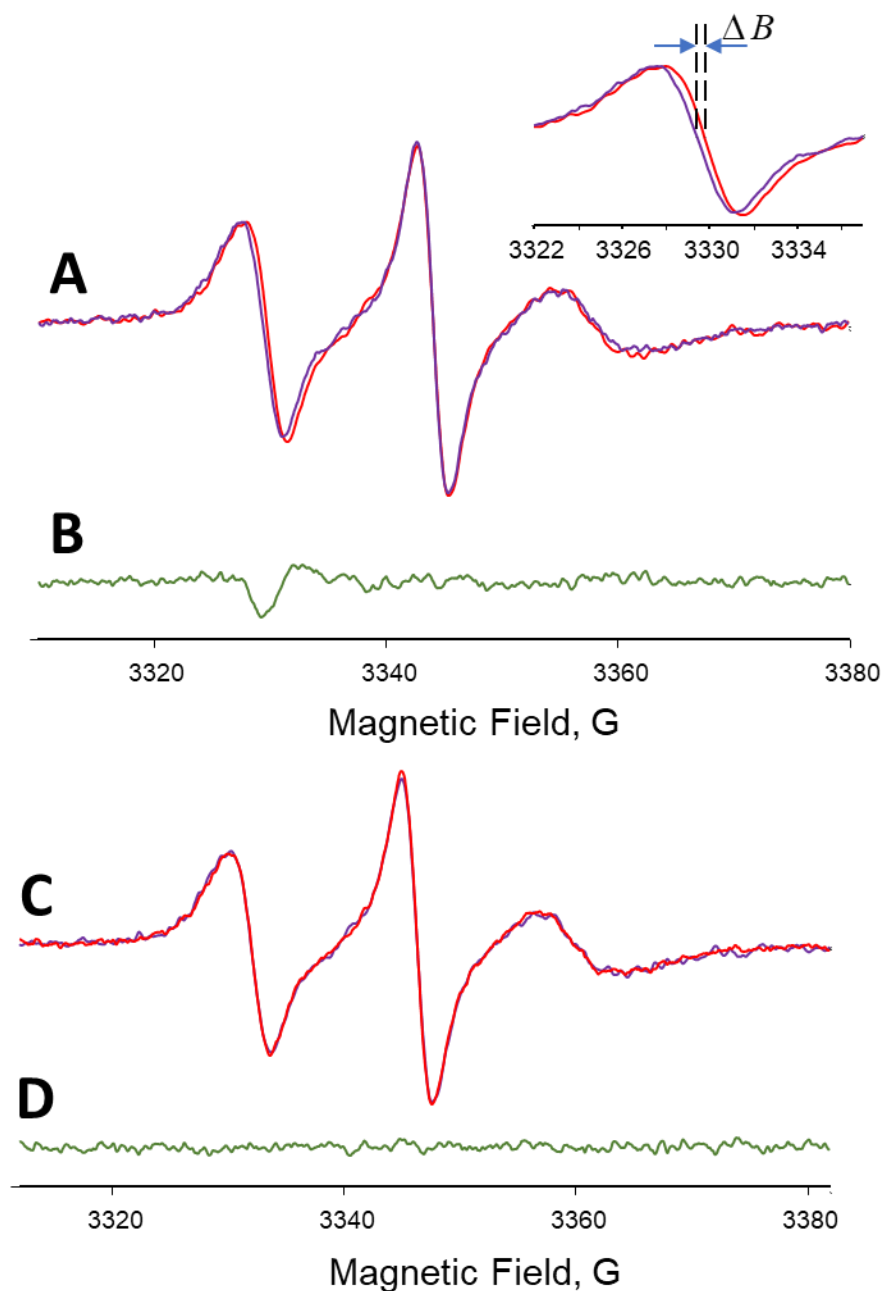
### 4.3.2. Characterization of the Nanoporous AAO Substrates and Lipid Deposition

Figure 4.02 shows representative SEM images of the back sides of two nanoporous AAO membranes fabricated for this study. The images reveal a heterogeneous ordered pore morphology that is untypical for the two-step anodization procedure as previously described in Chapter 1. The pore diameters were analyzed directly from these images using ImageJ. The pore diameters were determined to be  $\sim 38\text{ nm}$ .



**Figure 4.02** SEM images of top (A-B) and bottom (C-D) sides of the AAO substrate ( $d \approx 38$  nm, thickness =  $57 \mu\text{m}$ ).

With such small pore diameter, it was unclear if the lipid systems in fact, deposited within the nanopores. In order to confirm that the lipids deposited, EPR spectrum of the usual parallel orientation was compared to the spectrum of the perpendicular orientation (Figure 4.03). There was no change in the spectra suggesting that the lipids were deposited within the AAO nanopores.



**Figure 4.03** Effects of orientation of nanoporous AAO substrate with deposited nanotubular POPG lipid bilayers doped at 1 mol% with IMTSL-PTE vs. magnetic field on X-band EPR spectra. (A) A superposition of the spectra measured with magnetic field perpendicular (red) and parallel (magenta) to the static magnetic field shows small but noticeable changes in the average hyperfine splitting due to the sample macroscopic alignment. These changes are clearly seen at the insert showing a magnified low-field nitrogen hyperfine coupling component for the spectra aligned by the central ( $m_I=0$ ) hyperfine line. These orientation effects are expected to be small for the spin label attached to the lipid polar head via a flexible tether. (B) The difference between the spectra shown in (A) and aligned by adjusting isotropic g-factors and intensities by a least-squares procedure. (C) A consequent reorientation of the

*AAO substrate perpendicular to the magnetic field yielded an EPR spectrum identical to the one acquired initially: the red and magenta spectra are essentially indistinguishable when superimposed on one another and (D) the difference spectrum shows only random noise. The latter spectra show that minor misalignments of the AAO substrate with respect to magnetic field have no effects on the EPR spectra. All spectra were measured at 17 °C for lipid bilayers equilibrated at pH=7.00. For each of the orientations, 4 different spectra were measured, yielding identical results.*

### **4.3.3. Effect of Unannealed AAO Substrate on EPR spectra of Nanopore-confined Lipid**

#### **Bilayer**

A pH-sensitive nitroxide labeled at the headgroup of a phospholipid probe (IMTSL-PTE) (Figure 4.04), synthesized by the Smirnov group, was fully integrated into the lipid bilayer of POPG lipid deposited onto unannealed AAO substrate. The IMTSL-PTE probe undergoes reversible protonation at the tertiary amine that is not part of the nitroxide moiety, as shown in Figure 4.05, resulting in a localized positive charge. Then, a component of the positive internal electric field directed along the N-O bond will partially stabilize the nitrogen p orbital and destabilize the oxygen p orbital, leading to a partial shift of the spin density from N to O. This spin density change is reflected as magnetic parameters (such as the hyperfine coupling constant). Because of the electrostatics of the substrate-supported bilayer, fluctuations of charged and uncharged species occur, leading to changes in the ionization of the probe. By varying the pH, the induced changes in the acid-base equilibrium at the interface between the protonated and nonprotonated forms of the nitroxide are revealed. The protonated and nonprotonated forms have different rotational motions, and those forms can be detected from EPR spectra, reporting on the ionization state ( $pK_a$ ) of the probe.

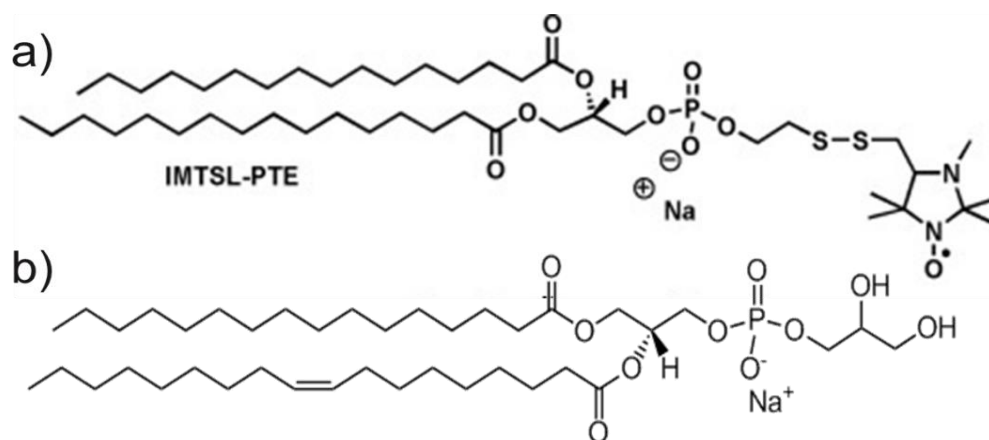


**Figure 4.04** Similar lipid structure of a) a spin-labeled probe and b) a POPG lipid.

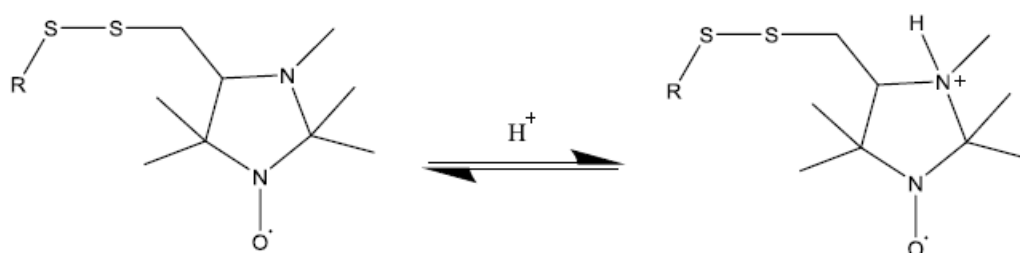


**Figure 4.05** Protonation of IMTSL-PTE at the interface of POPG MLVs. Reproduced from ref. [31].

A series of EPR spectra (normalized by frequency and intensity) of the IMTSL-PTE spin-labeled POPG nanotubular bilayers confined by unannealed AAO substrate as a function of bulk pH are displayed in Figure 4.06. The spectra are typical for nitroxides in intermediate to slow motion regimes and demonstrate that the spectral line shape is altered upon the adjustment of the bulk pH of the sample. An additional slow-motion spectral component began to appear in the low-field portion as the fraction of the protonated form of the probe increased upon lowering the pH. This slow-motion component was accompanied by a decrease of an intermediate motion component corresponding to the unprotonated nitroxide form.

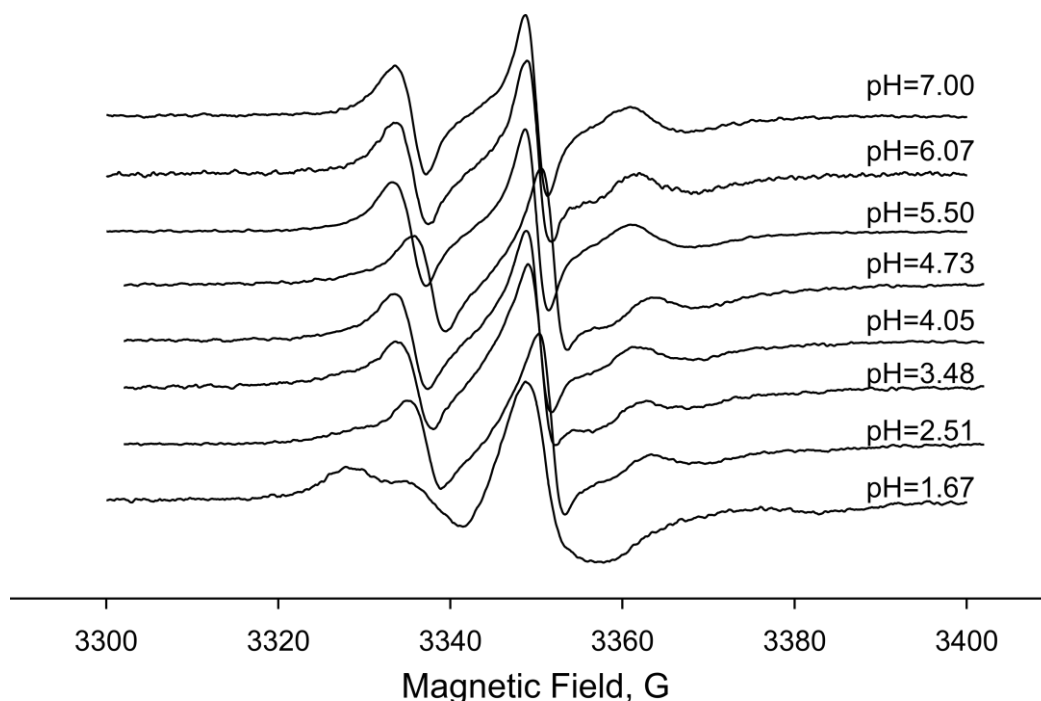


**Figure 4.06** X-band EPR spectra of AAO substrate-supported POPG doped with 1 mol% IMTSL-PTE acquired for various pH at 17 °C.

However, there was background EPR signal from the AAO substrate, causing an interference with both spectral components and thus disrupting the determination of the probe's pKa. Consequently, this AAO background signal had to be resolved with high-temperature treatment.

#### **4.3.4. High-Temperature Annealing of the AAO Substrate**

Figure 4.07 shows the spectra of the annealed AAO substrate at various high temperatures. As the temperature increases, the background signal of the AAO decreases. For 800 °C, the signal has significantly decreased, and thus, any high-temperature annealing above 800 °C will no longer affect the EPR spectra of the lipid bilayers within the pores. In this project, the AAO was annealed at 800 °C.

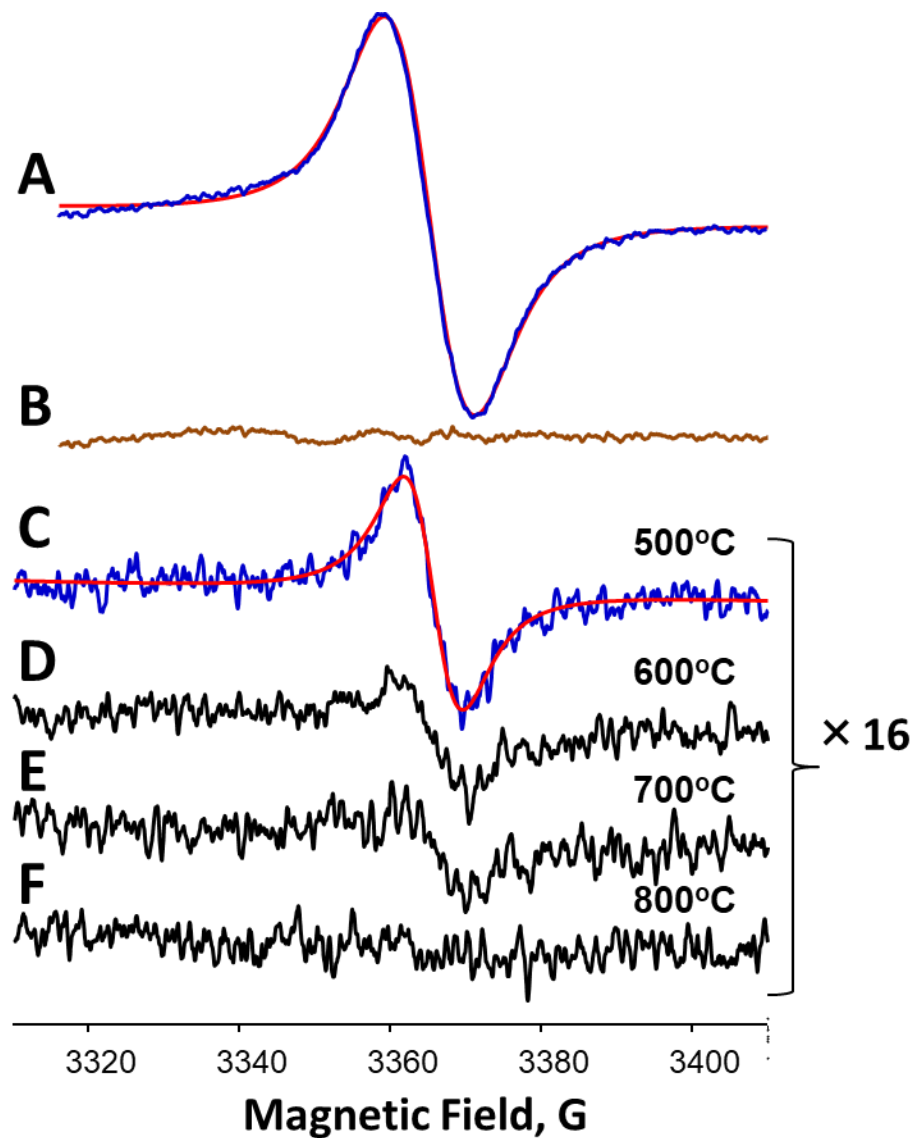


**Figure 4.07** Effect of high-temperature annealing of nanoporous AAO substrate (A) A superposition of the experimental unannealed AAO spectrum (red) and the unannealed AAO spectrum broadened to 3 Lorentzian points (blue); (B) The difference between the spectra shown in (A) and aligned by adjusting isotropic  $g$ -factors and intensities by a least-squares procedure. The red and blue spectra are essentially indistinguishable when superimposed on one another; (C)-(F) spectra measured after annealing the AAO substrate at each temperature. There is a decrease in the AAO background signal as the temperature increases.

#### 4.3.5. Determination of Surface Electrostatic Potential of Nanopore-confined POPG Lipid Bilayer in Annealed AAO Substrate

A series of EPR spectra (normalized by frequency and intensity) of the IMTSL-PTE spin-labeled POPG nanotubular MLVs confined by annealed AAO substrate for each bulk pH measured at 17 °C are displayed in Figure 4.08. The spectra are typical for nitroxides in intermediate to slow motion regimes and demonstrate that the spectral line shape is altered upon the adjustment of the bulk pH of the sample. An additional slow-motion spectral component began to appear in the low-field portion as the fraction of the protonated form of the probe increased upon lowering the pH. A decrease of an intermediate motion component corresponding to the unprotonated nitroxide form accompanied this slow-motion component.

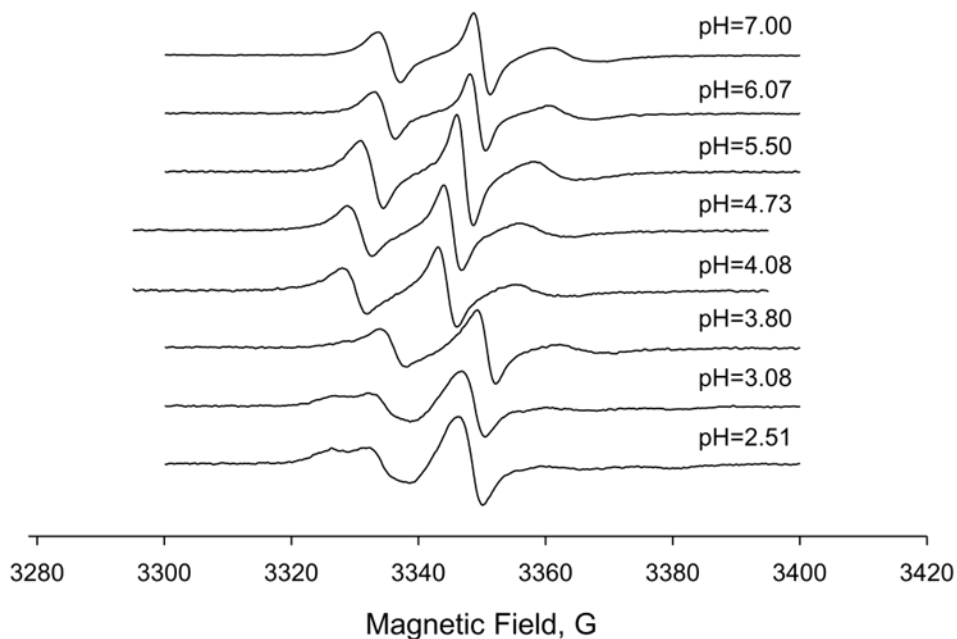


**Figure 4.08** X-band EPR spectra of nanopore-confined POPG lipids doped with 1 mol% IMTSL-PTE in AAO substrate annealed at 800 °C acquired for various pH at 17 °C.

Experimental EPR spectra were least-squares simulated as a superposition of spectra corresponding to pure unprotonated (highest pH spectra) and protonated (lowest pH spectra)

forms to determine the fraction of non-protonated component (Equation 4.3) using an EWVoigt program developed by Dr. Smirnov and the methods described in [1].

$$f = \frac{D(R)}{D(R)+D(RH^+)} \quad (4.3)$$

where  $D(R)$  is the double integral of the non-protonated component and  $D(RH^+)$  is the double integral of the protonated component. An example of this simulation for IMTSL-PTE labeled POPG in the AAO substrate at pH=4.08 is shown in Figure 4.09. The difference between the experimental and simulated spectra (or the residual of the superpositioning) is a straight line, which confirms the application of the pH-induced lipid mobility model.

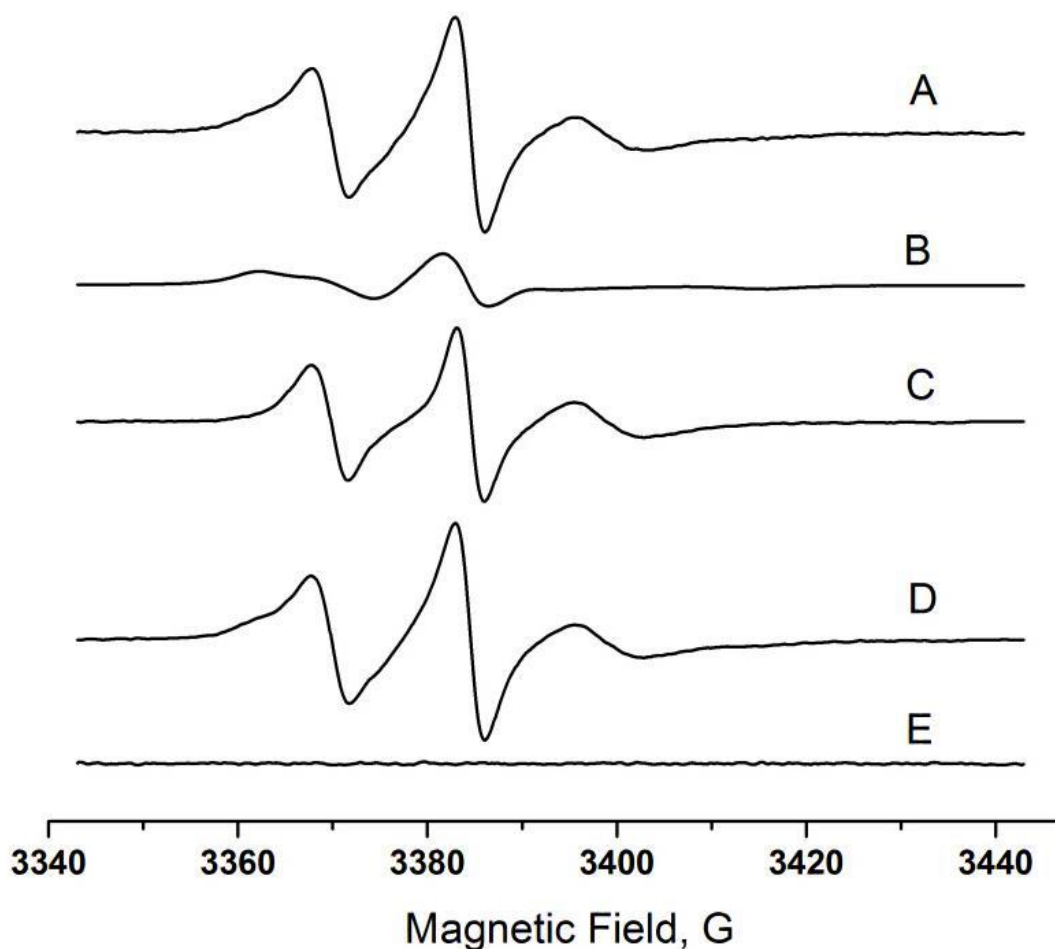


**Figure 4.09** Least-squares decomposition of the experimental X-band (9.5 GHz) EPR spectrum of IMTSL-PTE 1 mol%-doped POPG MLVs in annealed AAO at 800 °C acquired at pH=4.08 and 17 °C. (A) Experimental spectrum; Least-squares simulated spectra of (B) nonprotonated and (C) protonated forms of the nitroxide; (D) simulated spectrum; (E) residual of the fit. Adapted from ref. [31].

The experimentally determined fractions,  $f$ , were plotted vs. pH and fitted to a modified Henderson-Hasselbalch equation (Equation 4.4), yielding a titration curve (Figure 4.10).

$$f = \frac{10^{(pH-pK_a^i)}}{1+10^{(pH-pK_a^i)}} \quad (4.4)$$

where the  $pK_a$  is the interfacial  $pK_a^i$  of the probe. From this fitting, the interfacial  $pK_a^i$  was assessed to be  $pH = 4.08 \pm 0.08$ .

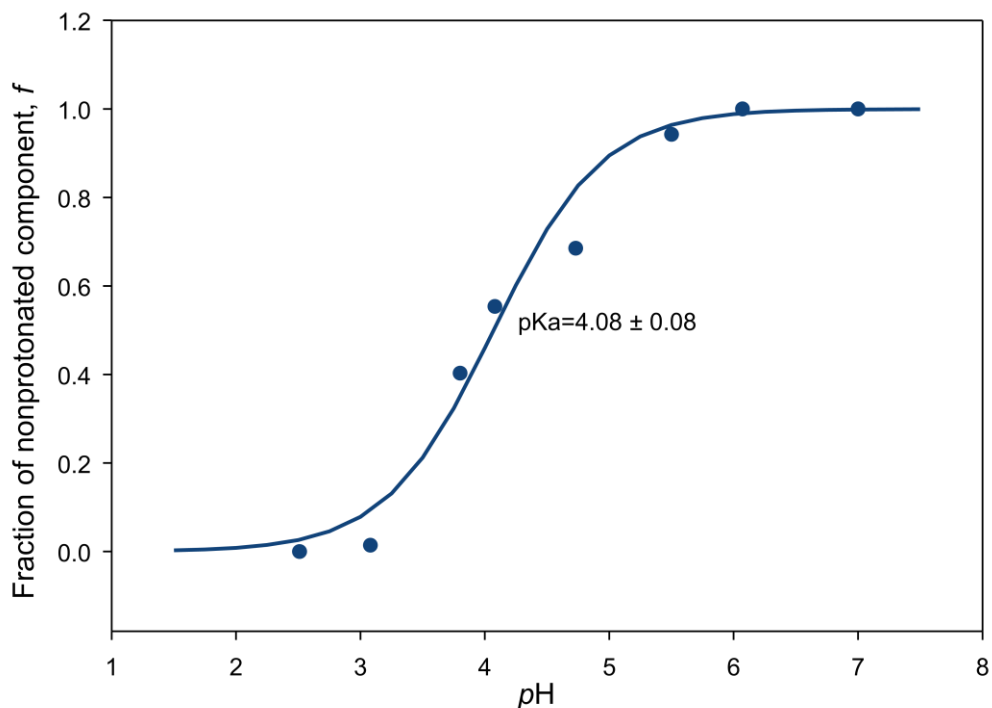


**Figure 4.10** Titration curve of annealed AAO substrate-supported POPG lipids doped with IMTSL-PTE at 17 °C.

Using the  $pK_a^i$  with the additive contributions of the interfacial polarity  $\Delta pK_a^{pol}$  and intrinsic  $pK_a^0$  previously determined in [1], the electrostatic term of IMTSL-PTE spin-labeled POPG was determined to be  $\Delta pK_a^{el} = 1.56 \pm 0.09$  from Equation 4.1. Subsequently, the surface electrostatic potential of the nanopore-confined bilayers can be evaluated as  $\Psi = -90 \pm 5$  mV in Equation 4.2. These electrostatic values determined for lipids in smaller, annealed nanopores (~38 nm) are lower than electrostatic values previously determined for unsupported POPG unilamellar vesicles (ULV) and MLVs with larger diameter (>45 nm) measured at 17 °C, which are shown in Table 4.01 (\*P<0.1, one-tailed Mann-Whitney test).

Typically, a decrease in the vesicle diameter (or increase of curvature) generates a local packing density of the lipid polar headgroups, which ultimately increases the surface potential (as exhibited in Table 4.01). Figure 4.11 similarly shows how increasing the size of the lipid vesicle decreases the surface potential.

**Table 4.01** Interfacial  $pK_a^i$ , polarity-induced and electrostatic shifts,  $\Delta pK_a^{el}$ , measured for POPG SUVs doped with 1% IMTSL-PTE at 17 °C. Data was reproduced from ref. [31].

Vesicle type	Diameter, nm	$pK_a^i$	$\Delta pK_a^{el}$	$\Psi$ , mV
ULV	49	$5.22 \pm 0.04$	$2.69 \pm 0.02$	$-155 \pm 1$
ULV	65	$5.02 \pm 0.06$	$2.50 \pm 0.07$	$-144 \pm 4$
ULV	107	$4.90 \pm 0.05$	$2.38 \pm 0.07$	$-137 \pm 4$
MLV	–	$5.49 \pm 0.03$	$2.97 \pm 0.05$	$-171 \pm 3$

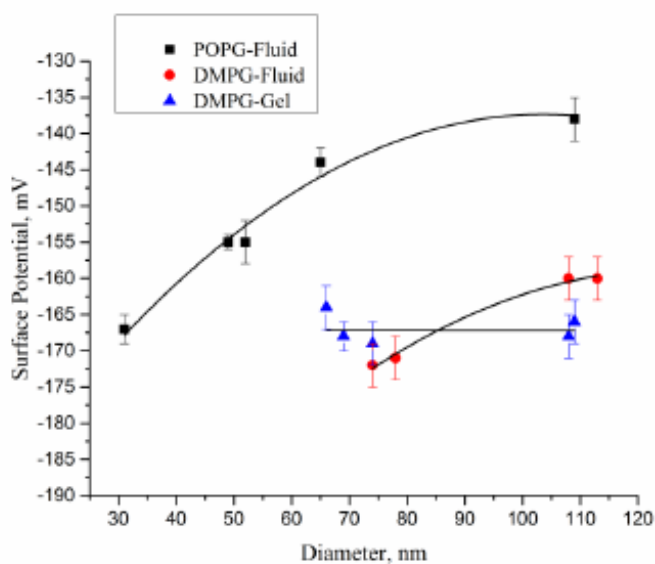


**Figure 4.11** Effect of curvature (vesicle diameter) on the surface electrostatic potential in lipid unilamellar vesicles. Reproduced from ref. [31].

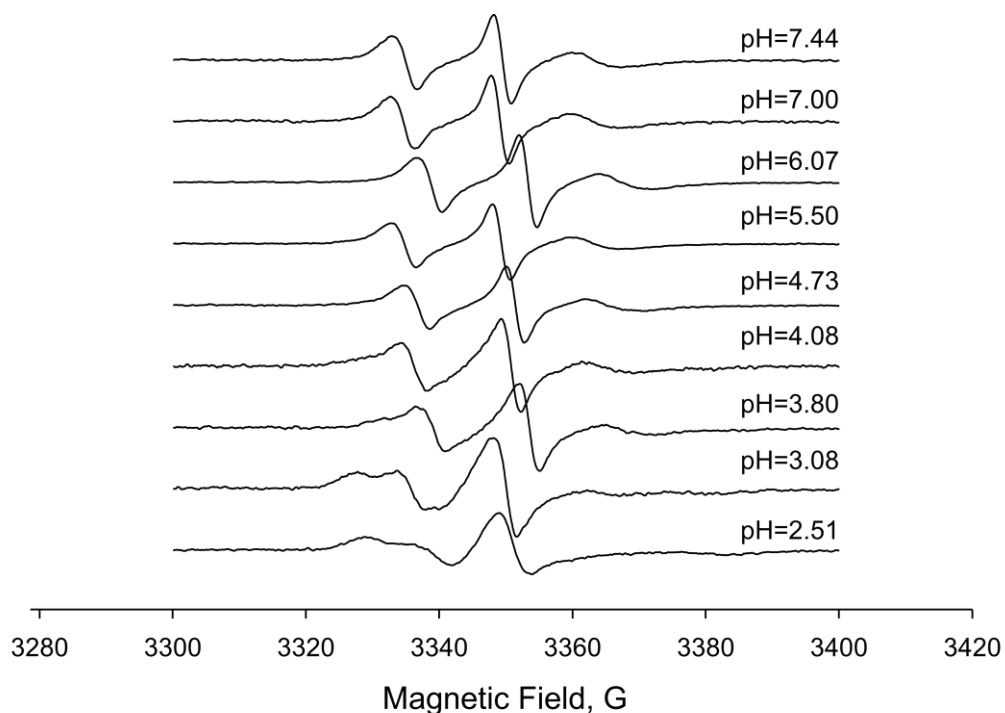
We speculate that the lower absolute values of the negative surface electrostatic potential of the lipids confined in the smaller ~38 nm nanopores is a direct consequence of electrostatic interactions of the lipids with the pore surface. Indeed, the preceding studies of even smaller annealed nanopores of ca. 18 and 29 nm in diameter indicated that pH inside the pores was about 0.5–0.8 pH unit lower than the bulk pH [32]. Furthermore, it was found that an increase in acidity of the bulk solution led to a steady decrease of the negative charge on inner surface of the ~38 nm nanopores and its recharge from a negative to a positive value at  $\text{pH } 4.7 \pm 0.1$ , corresponding to the point of zero charge (pzc). Thus, at  $\text{pH} = 4.08 \pm 0.08$ , the inner surface of the AAO pores is positively charged. This charge partially compensates for the larger negative surface potential of lipid bilayers, contributing to a lower surface electrostatic potential value overall.

#### **4.3.6. Determination of Surface Electrostatic Potential of Nanopore-confined POPG Lipid Bilayer Doped with Gramicidin A in Annealed AAO Substrate**

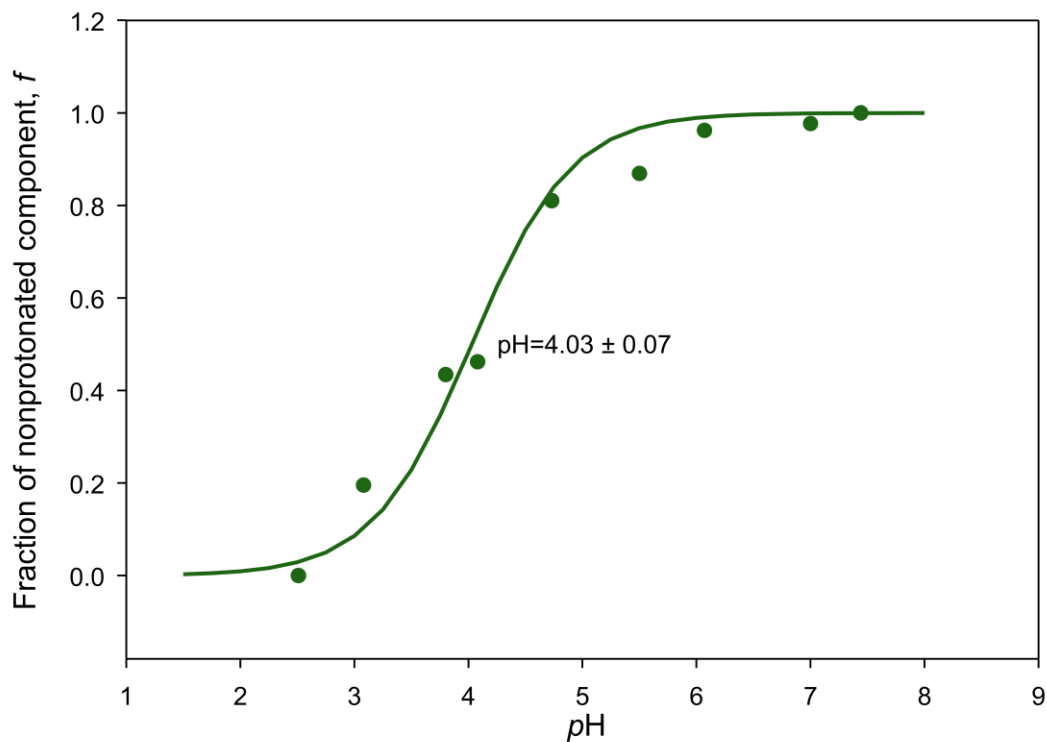
To facilitate a complete probe pH equilibration inside and outside of the lipid bilayer, a small ionophore, gramicidin A (gA), was inserted into the spin-labeled POPG MLVs to act as a proton channel [31]. In lipid bilayers, the gramicidin A dimerizes to form an ion channel to assure proton transfer on both sides of the formed lipid bilayer during buffer exchanges. POPG lipid doped with gA (1-3 channels per vesicle) and IMTSL-PTE (1 mol%) was titrated using the EPR titration method described earlier in section 4.3.5.

Figure 4.12 shows representative EPR spectra for the IMTSL-PTE spin-labeled POPG nanotubular MLVs doped with gA in annealed AAO substrate for each bulk pH measured at

17 °C. The corresponding titration curve (Figure 4.13) indicates that the interfacial  $pK_a^i$  of the nanopore-confined POPG lipids with gA is essentially the same that of the interfacial  $pK_a^i$  without gA (summarized in Table 4.02).



**Figure 4.12** X-band EPR spectra of nanopore-confined POPG lipids doped with 1 mol% IMTSL-PTE and gramicidin A in AAO substrate annealed at 800 °C acquired for various pH at 17 °C.



**Figure 4.13** Titration curve of annealed AAO substrate-supported POPG lipids doped with IMTSL-PTE and gramicidin A at 17 °C.

**Table 4.02** Interfacial  $pK_a^i$ , polarity-induced and electrostatic shifts,  $\Delta pK_a^{el}$ , measured for POPG SUVs doped with 1% IMTSL-PTE at 17 °C.

Vesicle type	$pK_a^i$	$\Delta pK_a^{el}$	$\Psi$ , mV
POPG	$4.08 \pm 0.08$	$1.56 \pm 0.09$	$-90 \pm 5$
POPG w/Gram	$4.03 \pm 0.07$	$1.51 \pm 0.08$	$-87 \pm 5$

These results show that the lipid bilayers formed inside AAO are rapidly (within a few minutes) re-equilibrated at a new pH value regardless of whether or not proton-conducting gramicidin A channel is present. This is likely due to a presence of defects on the pore surfaces that provide efficient pathway for protons to enter a thin water layer between the bilayer and the pore walls.

The data also indicate that after the lipid deposition, the pores remain open to small molecules and ions such as  $\text{H}^+$  [31-34].

#### **4.4. Conclusion**

The effect of high-temperature annealing of the AAO substrate on the surface electrostatic potential of the substrate-supported POPG lipids with IMTSL-PTE spin label was examined. Background signal of the substrate was removed by high-temperature annealing at 800 °C, which allowed for EPR titration and measurement of the nanopore-confined IMTSL-PTE spin-labeled POPG lipids. Each EPR spectrum was decomposed into the nonprotonated and protonated form, and the surface electrostatic potential was determined from the interfacial  $\text{p}K_a^i$  due to pH-induced changes. Specifically, nanopore-confined POPG demonstrated surface electrostatic potential significantly different from multilamellar vesicles by approximately 60 mV. It is likely that the positively charged inner surface of the AAO counterbalancing the negative surface electrostatic potential of the lipid MLVs is responsible for this substantial difference. However, with the addition of gramicidin A, these AAO substrate-supported POPG lipids with IMTSL-PTE showed small variations in the surface electrostatic potential. Thus, the nanopore-confined lipid bilayers completely re-equilibrated for each pH value.

By utilizing magnetic resonance approaches, such as this technique, more insight can be gained into the macromolecular dynamics of membrane lipids/proteins and, therefore, elucidate the potential for biotechnological applications, such as biosensors and biochips built with membrane proteins and receptor complexes.

#### 4.5. References

1. Voinov, M.A., I. Rivera-Rivera, and A.I. Smirnov, *Surface electrostatics of lipid bilayers by EPR of a pH-sensitive spin-labeled lipid*. Biophysical journal, 2013. **104**(1): 106-116.
2. Cevc, G., *Membrane electrostatics*. Biochimica et biophysica acta, 1990. **1031**(3): 311-382.
3. Cevc, G.; Marsh, D. *Phospholipid bilayers: physical principles and models*. 1987: Wiley.
4. Yang, Y.; Mayer, K. M.; Hafner, J. H. *Quantitative membrane electrostatics with the atomic force microscope*. Biophysical journal, 2007. **92**: 1966–1974.
5. Leonenko, Z.; Gill, S.; Amrein, M. *An elevated level of cholesterol impairs self-assembly of pulmonary surfactant into a functional film*. Biophysical journal, 2007. **93**: 674–683.
6. Marra, J. *Direct measurement of the interaction between phosphatidylglycerol bilayers in aqueous electrolyte solutions*. Biophysical journal, 1986. **50**: 815–825.
7. Fernandez, M. S.; Fromherz, P. *Lipoid pH indicators as probes of electrical potential and polarity in micelles*. Journal of physical chemistry, 1977. **81**: 1755–1761.
8. Rottenberg, H. *Determination of surface potential of biological membranes*. Methods in enzymology, 1989. **171**: 364–375.
9. Fromherz, P. *Lipid coumarin dye as a probe of interfacial electrical potential in biomembranes*. Methods in enzymology, 1989. **171**: 376–387.
10. Cafiso, D.; McLaughlin, A.; Winiski, A. *Measuring electrostatic potentials adjacent to membranes*. Methods in enzymology, 1989. **171**: 342–364.
11. Crowell, K. J.; MacDonald, P. M. *Surface charge response of the phosphatidylcholine head group in bilayered micelles from phosphorus and deuterium nuclear magnetic resonance*. Biochimica et biophysica acta. 1999. **1416**: 21–30.
12. Lindström, F.; Williamson, P. T. F; Gröbner, G. *Molecular insight into the electrostatic membrane surface potential by  $^{14}\text{N}/^{31}\text{P}$  MAS NMR spectroscopy: nociceptin-lipid association*. Journal of american chemical society, 2005. **127**: 6610–6616.
13. Barratt, M. D.; Laggner, P. *The pH-dependence of ESR spectra from nitroxide probes in lecithin dispersions*. Biochimica et biophysica. acta, 1974. **363**: 127–133.
14. Sanson, A.; Ptak, M.; Gary-Bobo, C. M. *An ESR study of the anchoring of spin-labeled stearic acid in lecithin multilayers*. Chemistry physics lipids, 1976. **17**: 435–444.

15. Bonnet, P.-A.; Roman, V.; Berleur, F. *Carboxylic acid or primary amine titration at the lipid-water interface: on the role of electric charges and phospholipid acyl chain composition. A spin labeling experiment*. Chemistry physics lipids, 1990. **55**: 133–143.
16. Sankaram, M. B.; Brophy, P. J.; Marsh, D. *Fatty acid pH titration and the selectivity of interaction with extrinsic proteins in dimyristoylphosphatidylglycerol dispersions-spin label ESR studies*. Biochimica et biophysica. acta, 1990. **1021**: 63–69.
17. Shin, Y. K.; Hubbell, W. L. *Determination of electrostatic potentials at biological interfaces using electron-electron double resonance*. Biophysical journal, 1992. **61**: 1443–1453.
18. Marquezin, C. A.; Hirata, I. Y.; Ito, A. S. *Spectroscopic characterization of 2-amino-n-hexadecyl-benzamide (AHBA), a new fluorescence probe for membranes*. Biophysical chemistry, 2006. **124**: 125–133.
19. Riske, K. A.; Nascimento, O. R.; Lamy-Freund, M. T. *Probing DMPG vesicle surface with a cationic aqueous soluble spin label*. Biochimica et biophysica acta, 1999. **1418**: 133–146.
20. Khrantsov, V. V.; Marsh, D.; Reznikov, V. A. *The application of pH-sensitive spin labels to studies of surface potential and polarity of phospholipid membranes and proteins*. Biochimica et biophysica acta, 1992. **1104**: 317–324.
21. Fernandez, M. S.; Fromherz, P. *Lipoid pH indicators as probes of electrical potential and polarity in micelles*. Journal of physical chemistry, 1977. **81**: 1755–1761.
22. Fromherz, P. *Lipid coumarin dye as a probe of interfacial electrical potential in biomembranes*. Methods in enzymology, 1989. **171**: 376–387.
23. Bonnet, P.-A.; Roman, V.; Berleur, F. *Carboxylic acid or primary amine titration at the lipid-water interface: on the role of electric charges and phospholipid acyl chain composition. A spin labeling experiment*. Chemistry physics lipids. 1990. **55**: 133–143.
24. Voinov, M.A., Kirilyuk, I.A.; Smirnov, A.I. *Spin-labeled pH-sensitive phospholipids for interfacial pKa determination: synthesis and characterization in aqueous and micellar solutions*. Journal of physical chem B, 2009. **113**(11): 3453-60.
25. Kovaleva, E. G.; et al. *Electrostatic properties of inner nanopore surfaces of anodic aluminum oxide membranes upon high temperature annealing revealed by EPR of pH-sensitive spin probes and labels*. Journal of membrane science, 2020. **604**: 118084.
26. Masuda, H.; Fukuda, K. *Ordered Metal Nanohole Arrays Made by a Two-Step Replication of Honeycomb Structures of Anodic Alumina*. Science, 1995. **268**: 1466-1468.

27. Alaouie, A. M.; Smirnov, A. I. *Ultra-stable temperature control in EPR experiments: thermodynamics of gel-to-liquid phase transition in spin-labeled phospholipid bilayers and bilayer perturbations by spin-labels*. *Journal of magnetic resonance*, 2006. **182**: 229–238.
28. Seelig, J.; MacDonald, P. M.; Scherer, P. G. *Phospholipid head groups as sensors of electric charge in membranes*. *Biochemistry*, 1987. **26**: 7535–7541.
29. Heimburg, T.; Biltonen, R. L. *Thermotropic behavior of dimyristoylphosphatidylglycerol and its interaction with cytochrome C*. *Biochemistry*, 1994. **33**: 9477–9488.
30. Biaggi, M.H.; Riske, K. A.; Lamy-Freund, M. T. *Melanotropic peptides-lipid bilayer interaction. Comparison of the hormone  $\alpha$ -MSH to a biologically more potent analog*. *Biophysical chemistry*, 1997. **67**: 139–149.
31. Fernandez, R.M., Lamy-Freund, M. T. *Correlation between the effects of a cationic peptide on the hydration and fluidity of anionic lipid bilayers: a comparative study with sodium ions and cholesterol*. *Biophysical chemistry*, 2000. **87**: 87–102.
32. Silvius, J. R. *Thermotropic phase transitions of pure lipids in model membranes and their modifications by membrane proteins*. In *Lipid-protein interactions*. P. C. Jost, and O. H. Griffith, editors. 1982. John Wiley & Sons/New York.
33. Zhao, W.; et al. *Atomic-Scale Structure and Electrostatics of Anionic Palmitoyloleoylphosphatidylglycerol Lipid Bilayers with Na<sup>+</sup> Counterions*. *Biophysical journal*, 2007. **92**(4): 1114-1124.
34. Koolivand, A. *Dynamics, Surface Electrostatics and Phase Properties of Nanoscale Curved Lipid Bilayers*. 2015, <http://www.lib.ncsu.edu/resolver/1840.16/10620>.

## APPENDICES

## Appendix A

As described in Chapter 3, a least squares simulation method was utilized to determine the fraction of the non-protonated nitroxide species,  $f$ . Specifically, an experimental EPR spectrum at an intermediate pH,  $I(B)$ , was modeled as a superposition of spectra from the non-protonated and protonated species,  $F_R(B)$  and  $F_{RH^+}(B)$ , respectively:

$$I(B) = a \cdot F_R(B) + b \cdot F_{RH^+}(B) \quad (1)$$

For the simulation procedure,  $F_R(B)$  and  $F_{RH^+}(B)$  spectra could be measured experimentally and then used for spectral decomposition to derive the coefficients  $a$  and  $b$ . The fraction of the non-protonated form of the nitroxide,  $f = a \cdot D_R / (a \cdot D_R + b \cdot D_{RH^+})$ , is then calculated from the double integrals  $D_R$  and  $D_{RH^+}$  of the corresponding  $F_R(B)$  and  $F_{RH^+}(B)$  spectra and the coefficients  $a$  and  $b$ . However, some of the experimental EPR spectra could contain an intermixture of an out-of-phase EPR signal and also may have shifted in the magnetic field due to a change in the resonator frequency. To account for these factors, convolution filtering was employed to aid in the correction of the phase distortion by digital convolution with a Lorentzian function of the desired phase (S1). Specifically, the phase shift  $\Delta\phi$  and  $\Delta\phi_+$ , magnetic field  $\Delta B$  and  $\Delta B_+$  parameters, and the intensity coefficients  $a$  and  $b$  were adjusted during the least-squares Levenberg–Marquardt optimization to minimize:

$$I(B) \otimes L(0,0,\Delta B_{pp}) - \{a \cdot F_R(B) \otimes L(\Delta B_R, \Delta\phi_R, \Delta B_{pp}) + b \cdot F_{RH^+}(B) \otimes L(\Delta B_{RH^+}, \Delta\phi_{RH^+}, \Delta B_{pp})\} \rightarrow 0 \quad (2)$$

where the operator  $\otimes$  is for the convolution integral and  $L(\Delta B_i, \Delta\phi_i, \Delta B_{pp})$  are the Lorentzian functions of the peak-to-peak width,  $\Delta B_{pp}$ , the phase shift from pure absorption,  $\Delta\phi_i$ , and the magnetic field shift,  $\Delta B_i$ . This convolution fitting allows for adjustment of the phase and field position misalignments by varying parameters of the corresponding Lorentzian functions that

are determined analytically while  $F_R(B)$  and  $F_{RH^+}(B)$  are measured experimentally. Typically, the parameter  $\Delta B_{pp}$  (which should be the same for all three Lorentzian functions in expression (S2)) was set to be equal to three digitizing intervals of an EPR spectrum.

For this spectral simulation method, the reference spectra for the protonated and non-protonated nitroxide forms of the spin probe are required. Experimental EPR spectra are measured for pH increments of approximately 0.5 pH units in the pH intervals below and above the estimated (or expected)  $pK_a$  of the probe and then compared. If there are no measurable changes observed in two consecutive spectra taken at the most acidic (lowest) pH value, either spectrum could be used as a reference spectrum for  $F_{RH^+}(B)$ . The reference spectrum was selected for  $F_R(B)$  by repeating a similar procedure for EPR spectra recorded at the least acidic (highest) pH value above the probe  $pK_a$ .

The experimental EPR spectra were least-squares simulated as a superposition of the reference spectra corresponding to highest pH spectra (pure unprotonated) and lowest pH (protonated spectra) forms to determine the fraction of non-protonated component using an EWVoigt program developed by Dr. Smirnov and the methods described in (S3). An example of this simulation for IMTSL-PTE labeled POPG nanotubular bilayers in the AAO substrate at pH=4.08 is shown in Figure 4.09. The difference between the experimental and simulated spectra (or the residual of the superposition) is a straight line, which confirms the application of the pH-induced lipid mobility model.

## References

- S1. Cevc, G. *Phospholipids Handbook*. 1993. Marcel Dekker, New York.
- S2. Smirnov, A. I. *Post-processing of EPR spectra by convolution filtering: calculation of harmonics' series and automatic separation of fast motion components from spin-label EPR spectra*. *Journal of magnetic resonance*, 2008. **190**:154–159.
- S3. Voinov, M.A., I. Rivera-Rivera, and A.I. Smirnov, *Surface electrostatics of lipid bilayers by EPR of a pH-sensitive spin-labeled lipid*. *Biophysical journal*, 2013. **104**(1): 106-116.